Lab on a Chip

CRITICAL REVIEW

View Article Online
View Journal | View Issue

Cite this: *Lab Chip*, 2023, **23**, 1097

Applications of magnetic and electromagnetic forces in micro-analytical systems

M. Suwa, *[a] S. Tsukahara [a] and H. Watarai *[b]

Novel applications of magnetic fields in analytical chemistry have become a remarkable trend in the last two decades. Various magnetic forces have been employed for the migration, orientation, manipulation, and trapping of microparticles, and new analytical platforms for separating and detecting molecules have been proposed. Magnetic materials such as functional magnetic nanoparticles, magnetic nanocomposites, and specially designed magnetic solids and liquids have also been developed for analytical purposes. Numerous attractive applications of magnetic and electromagnetic forces on magnetic and non-magnetic materials have been studied, but fundamental studies to understand the working principles of magnetic forces have been challenging. These studies will form a new field of magneto-analytical science, which should be developed as an interdisciplinary field. In this review, essential pioneering works and recent attractive developments are presented.

Received 28th July 2022,
Accepted 25th November 2022

DOI: 10.1039/d2lc00702a

rsc.li/loc

1. Introduction

The book "Unified Separation Science", written by J. C. Giddings in 1991 not only introduced his original method of field-flow-fractionation but also greatly helped to understand the fundamental science behind various types of traditional separation methods by showing the concept of general driving forces in separation mechanisms of molecules and particles.[1] His basic idea is that the fundamental meaning of separation is physical displacement through space, which includes flow displacement that is powerful and nonselective and relative displacement that is relatively weak but selective for analytes.[2] Relative displacement needs a driving force, F, which is derived from the total chemical potential, μ^*, composed of physical interaction with an external field, μ_{ext},

[a] *Department of Chemistry, Graduate School of Science, Osaka University, Toyonaka, Osaka 560-0043, Japan. E-mail: msuwa@chem.sci.osaka-u.ac.jp*
[b] *R^3 Institute for Newly-Emerging Science Design, Osaka University, Toyonaka, Osaka 560-8531, Japan. E-mail: watarai@chem.sci.osaka-u.ac.jp*

Masayori Suwa

Masayori Suwa was born in Osaka in 1977. He graduated from the School of Science, Osaka University, in 2000 and received a D.S. Degree from the Graduate School of Science, Osaka University, under the supervision of Prof. Hitoshi Watarai in 2005. He became an Assistant Professor at Osaka University in 2005. He received The Japan Society for Analytical Chemistry Award for Young Researchers in 2009. He has been developing magneto-analytical techniques for micro/nanoparticles, for example, magnetophoretic velocimetry, magneto-optical microscopy under a pulsed magnetic field, and optical measurement of Brownian rotation of magnetic nanoparticles under an AC magnetic field.

Satoshi Tsukahara

Satoshi Tsukahara was born in Ibaraki in 1964. He graduated from the School of Science, Tohoku University in 1986 and received a Doctor of Science Degree from the Graduate School of Science, Tohoku University, under the supervision of Professor Nobuo Suzuki in 1993. He became a Professor at Osaka University in 2011. He received The Japan Society for Analytical Chemistry Award for Young Researchers in 1998. He is deeply interested in the physical and chemical phenomena at liquid/liquid interfaces and the extreme measurements of the phenomena occurring there.

and chemical interaction between a solute and solvent molecules, $\mu = \mu^\circ + RT\ln c$, where μ° is the standard chemical potential in the standard state and c is the concentration of the solute,

$$F = -\frac{\mathrm{d}(\mu_{\mathrm{ext}} + \mu^\circ)}{\mathrm{d}x} - RT\frac{\mathrm{d}\ln c}{\mathrm{d}x} \quad (1)$$

The last term indicates the diffusion of the solute. Based on this concept, he explained various possibilities for using different external fields to achieve separation schemes, such as thermophoresis, diffusiophoresis, photophoresis, dielectrophoresis, and magnetophoresis. These migration schemes were partly investigated but not significantly developed in analytical chemistry at that time. Among these, magnetophoresis requires magnets to generate a magnetic field gradient, but the handling of magnets was not much familiar for separation chemists, although NMR and ESR were commonly used in chemistry, and the high gradient magnetic separation (HGMS) method was already used in industry.[3] It can be recalled that the invention of new types of magnets in 1980s, for example, the strong permanent magnet of Nd–Fe–B by Sagawa (1984)[4] and cryogen-free superconducting magnet suggested by Hoenig (1983),[5] and their commercialization after a few years encouraged researchers to use these new types of magnets in various fields of science and technology.

According to magnetism, materials can be roughly classified into diamagnetic and paramagnetic materials, which are characterized by different magnetization profiles and magnetic susceptibilities.[6] Almost all organic and biological materials are diamagnetic and have negative magnetic susceptibilities, while some transition metals and lanthanides and their compounds are paramagnetic, having positive magnetic susceptibilities. The major forces exerted on a substance by the application of a magnetic field are shown in Fig. 1. The first one is Kelvin force (Fig. 1A), F_{K}, which is also known as the magnetic field-gradient force, given by the following equation, when it works on a spherical particle with volume, V:

$$F_{\mathrm{K}} = \frac{\chi_{\mathrm{p}}}{2\mu_0} V\nabla B^2 \quad (2)$$

where χ_{p} is the volume magnetic susceptibility of the particle, μ_0 is the permeability of free space ($4\pi \times 10^{-7}$ T mA^{-1}), $\nabla = \left(\frac{\partial}{\partial x}, \frac{\partial}{\partial y}, \frac{\partial}{\partial z}\right)$ is a vector differential operator, B is the magnetic flux density (T) and $\nabla B^2 = 2(B\cdot\nabla)B$. This force is used as the driving force of magnetophoresis. The second one is the torque (Fig. 1B), T, or magnetic orientation force, which is represented by,

$$T = m \times B \quad (3)$$

where m is the magnetic moment in a homogeneous magnetic field. Commonly, the term magnetic force means the magnetic gradient force and/or the magnetic torque. When two particles are magnetically oriented on a one-dimensional axis, a magnetic dipole–dipole interaction works between the particles depending on the distance and the directions of magnetic moments. They may form a head to tail associate or be separated with a balanced distance due to magnetic dipole repulsion depending on the magnetic field direction (Fig. 1C). The third one is the electromagnetic force or Lorentz force (Fig. 1D), F_{L}, which is generated perpendicular to the magnetic field and the electric or ionic current:

$$F_{\mathrm{L}} = qv \times B \quad (4)$$

where q is the charge of a particle moving with velocity v. In real magnetic systems, these four forces may work multiply depending on the situation. The contents of this review include (1) the application of magnetic force for the magnetophoresis of microparticles, manipulation and separation of micro/nanoparticles, dynamic force measurement of chemical interaction, solid phase and liquid phase extraction, and soft-robot and micro-composites, (2) the application of magnetic torque by dc and ac magnetic field for diamagnetic and paramagnetic particles, and (3) the application of electromagnetic force for electromagnetophoresis, dynamic force measurements, and electrochemical systems. Some topics relate to new types of magnetic materials, colloidal interaction systems and spin selectivity in electrochemical processes. There are many reviews in the literature concerning the use of magnetic forces in analytical chemistry.[7–11] Especially, the application of magnetic nanoparticles or nanocomposites have become an emerging topic.[12–22] In this review article, we revisit some pioneering works briefly, and then introduce recent attractive studies in the last two decades on the applications of magnetic forces and electromagnetic forces in the broad field of analytical chemistry. Finally, we comment on the prospects of this new field of magneto-analytical science.

Hitoshi Watarai

Hitoshi Watarai is an Emeritus Professor at Osaka University (2010) and he is now studying "magneto-analytical science" as an Invited Professor at the R³ Institute for Newly-Emerging Science Design, Osaka University. He obtained his MSc in Physical Chemistry (1971), PhD in Analytical Chemistry (1978) and he was employed as a Research Associate (1971) at Tohoku University. In 1981–1982 he worked in Prof. Henry Freiser's laboratory at the University of Arizona, where he started "nanochemistry at liquid–liquid interface". He became a Lecturer (1982), Associate Professor (1983) and Professor (1988) at Akita University. In 1993, he was transferred to Osaka University.

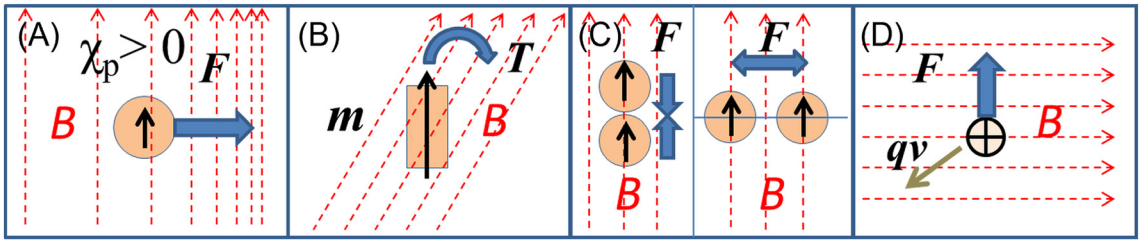

Fig. 1 Illustration of (A) Kelvin force, (B) magnetic torque, (C) typical magnetic dipole–dipole interactions and (D) Lorentz force.

2. Application of magnetic field-gradient force

2.1 Magnetophoresis

Magnetophoresis is the phenomenon in which a particle migrates with translational motion under a magnetic field gradient. Understanding the magnetophoretic behavior of individual particles is crucial for microfluidic magnetic separation, magnetic manipulation, magnetic drug targeting, *etc.* Here, we briefly introduce the fundamental principle of magnetophoresis.

Under a magnetic field gradient, ∇H, a magnetic force, F_{mag}, works on a particle,[23] as follows:

$$F_{mag} = \mu_m m \cdot \nabla H, \tag{5}$$

where μ_m is the magnetic permeability of the medium surrounding the particle and m is the magnetic dipole moment of the particle. The magnetization, M, of a weak magnetic (paramagnetic or diamagnetic) object is proportional to the external magnetic field, H, $M = \chi H$, where χ is the volume magnetic susceptibility of the object. The effective dipole moment, m_{eff}, of a spherical particle in a fluid can be expressed as follows:

$$m_{eff} = \left(\frac{\mu_p - \mu_m}{\mu_p + 2\mu_m}\right) VH, \tag{6}$$

where V is the volume of the particle and μ_p is the magnetic permeability of the particle. The relation between the magnetic permeability, μ, and the volume magnetic susceptibility, χ, is given by $\mu = (1 + \chi)\mu_0$ with the permeability of the vacuum, μ_0. The value of χ is in the order of 10^{-3}–10^{-6}, and therefore $\mu \approx \mu_0$. The relation between H and the magnetic flux density, B, is $B = \mu_0(H + M)$. Hence, in the case of weak magnetic materials, $B \approx \mu_0 H$. Consequently, the magnetic force on a spherical weak magnetic particle can be expressed as follows:

$$F_{mag} = \frac{\left(\chi_p - \chi_m\right)}{2\mu_0} V \nabla B^2. \tag{7}$$

This is the driving force of the magnetophoresis of a particle. The magnetic force is balanced with the viscous drag force given by

$$F_{drag} = 6\pi\eta r v_{mag}, \tag{8}$$

where r is the radius of the particle and v_{mag} is the magnetophoretic velocity. Therefore, the magnetophoretic velocity can be expressed as follows:

$$v_{mag} = \frac{1}{9}\frac{\left(\chi_p - \chi_m\right)}{\mu_0 \eta} r^2 \nabla B^2. \tag{9}$$

Thus, the magnetophoretic velocity is proportional to the difference in χ between the particle and medium, the square radius, and the gradient of B^2. If the particle is more paramagnetic than the medium ($\chi_p > \chi_m$), the particle moves toward the direction in which B^2 increases. In the opposite case ($\chi_p < \chi_m$), the particle migrates to avoid a stronger field. From the measurement of the velocity v_{mag}, the value of χ_p can be obtained if the other parameters are known. Then, the components in the particle can be evaluated, given that the value of χ_p is assumed to be the fractional sum of the magnetic susceptibilities of the components.

2.1.1 Magnetophoresis of single microparticles. Although magnetic separation had been used in the manufacturing and mining industries since the 19th century, there were only a few attempts to investigate the magnetophoretic velocity of small particles up to the late 1990s. The pioneering work was done by Gill *et al.*[24] They designed an apparatus to observe the magnetophoretic velocity of microparticles under a large inhomogeneous magnetic field of 4×10^3 T^2 m^{-1} in ∇B^2 between asymmetric pole pieces of an electromagnet. They suggested determining the magnetic susceptibilities of polystyrene latex particles and red blood cells from their magnetophoretic velocities measured with an optical microscope. Zborowski *et al.*[25] proposed a unique approach to estimate the average magnetic susceptibility of ferritin microparticles from their fraction in the elution of a flow magnetic separator.

The development of image processing techniques and strong magnets made it easy to directly measure the magnetophoretic velocity of microparticles. In the late 1990s and 2000s, fundamental and feasibility studies on magnetophoresis have been actively conducted. The research group of Zborowski and Chalmers played an important role in the development of magnetophoretic velocity analysis. Chalmers *et al.*[26,27] applied a computer algorithm, "cell tracking velocimetry (CTV)", to measure the magnetophoretic velocity of microparticles.[28–31] To estimate the magnetic susceptibility from the magnetophoretic velocity, the size of

the migrating particle should be measured. However, the precise size measurement is difficult because of the displacement of the particles from the focal plane of the microscope or the variation in the intensity of the illumination light. Thus, to solve this problem, Jin *et al.*[32] simultaneously measured the magnetophoretic velocity, v_{mag}, and sedimentation velocity, v_{sed}, with CTV. As shown in Fig. 2A, the magnetic force is perpendicular to the gravity in their setup, and thus v_{mag} and v_{sed} can be independently measured. Dividing v_{mag} by v_{sed} yields

$$\frac{v_{mag}}{v_{sed}} = \frac{\left(\chi_p - \chi_m\right)}{\left(\rho_p - \rho_m\right)g}\frac{\nabla B^2}{2\mu_0}. \quad (10)$$

where g is the acceleration of gravity and ρ_p and ρ_m are the densities of the particle and medium, respectively. Eqn (10) is independent of the radius, r, and the viscosity, η, and χ_p can be estimated from this equation, knowing the other parameters. An electromagnet is equipped to vary the strength of the magnetic field (B_{max} = 1.2 T, ∇B_{max}^2 = 150 T^2 m^{-1}). Fig. 2B shows an example of the CTV analysis. The most remarkable advantage of the magnetophoretic velocity analysis is that the distribution of the magnetic susceptibility of the cells is obtained. For the reliable measurement of the magnetic susceptibility of red blood cells (RBCs) with a SQUID magnetometer, 5000 cells are needed,[33] and then only the mean value can be determined. Alternatively, the magnetophoretic method can determine the magnetic susceptibility of individual red blood cells with a resolution of 1×10^7 Hb molecules per cell (4–5 fg of Fe). They measured the magnetophoretic velocity of deoxygenated RBCs after 14, 28, and 42 days of storage (Fig. 2C). The population shifted to a lower velocity, indicating the loss of Hb in RBC due to aging. In addition, they observed iron storage in circulating monocytes,[34,35] the relation between phosphatidylserine expression and magnetic mobility,[36] enzymatic deoxidation of Hb,[37] iron transport in cancer cells,[38] and showed the possibility of hematology analyzer detection.[39,40]

Watarai's group also contributed to the development of analytical techniques utilizing magnetophoresis. They

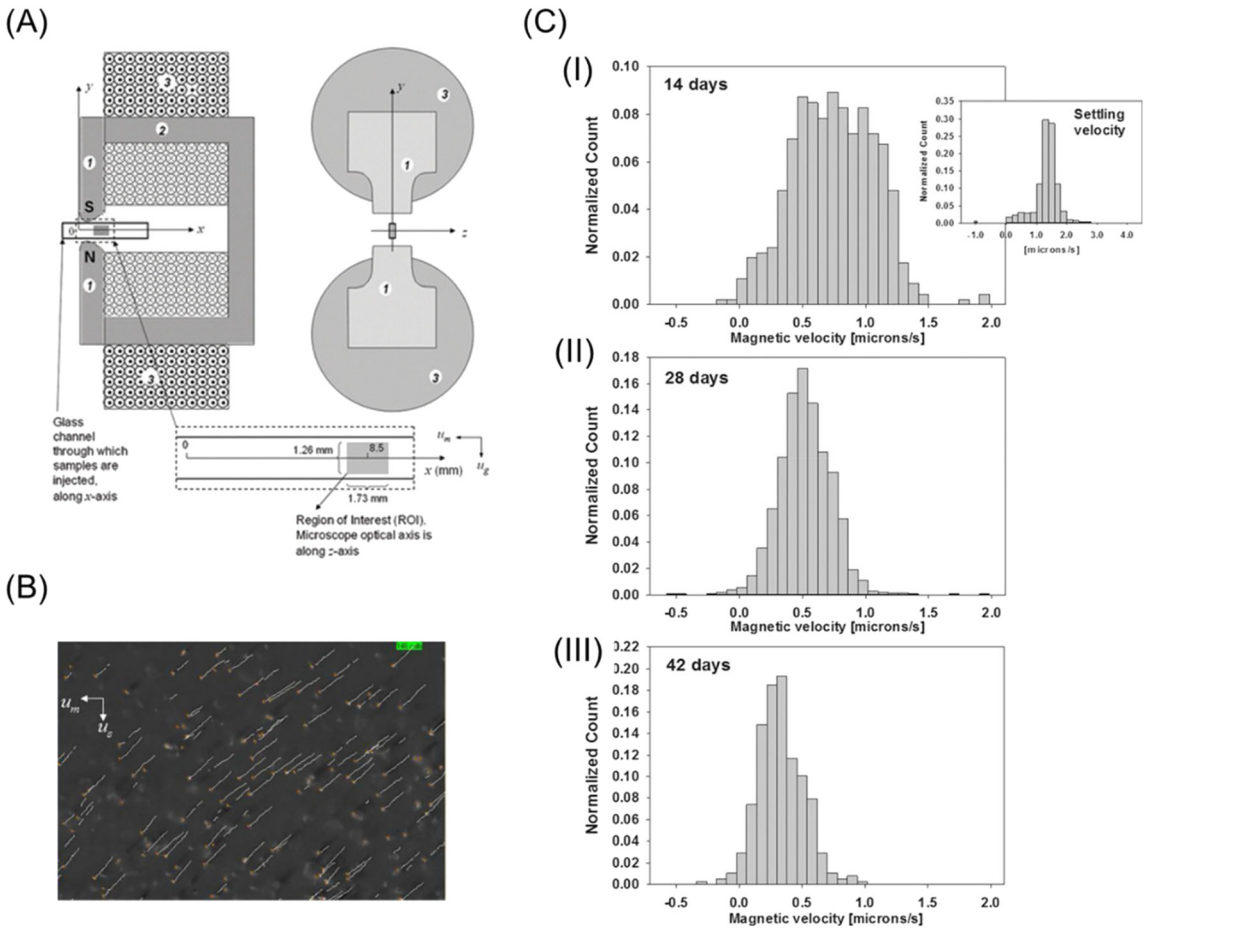

Fig. 2 (A) Schematic drawing of magnets and migration channel for the CTV system. 1 and 2 pole pieces and flux return yolk and 3 coil of the electromagnets. Reproduced from ref. 32 with permission from the Royal Society of Chemistry. (B) Screen output of CTV software of metHb RBC. Reproduced with permission from ref. 41 from the Royal Society of Chemistry. (C) Histograms of the magnetophoretic velocity of deoxygenated RBCs for the same specific donor after 14 (I), 28 (II), and 42 (III) days of storage. For comparison, the right panel of (I) shows a histogram of the settling velocity of RBCs at 14 days reprinted with permission from ref. 42. Copyright © 2017, the American Chemical Society.

investigated the magnetophoretic velocities of diamagnetic polystyrene microparticles in paramagnetic manganese(II) aqueous solution, *i.e.*, $\chi_p < \chi_m$.[43] As predicted by eqn (9), the reverse of the migration direction was experimentally observed for the first time. In this study, a capillary cell was set between a pair of Nd–Fe–B magnets. From the magnetophoretic velocity of a polystyrene microparticle, the complex profile of ∇B^2 at the edge of the magnet could be determined. Suwa and Watarai constructed an apparatus for the sensitive measurement of the magnetophoretic velocity utilizing a superconducting magnet (10 T). By placing a silica capillary cell between a pair of iron pole pieces in the bore of the superconducting magnet, a very large gradient field (maximum of $\nabla B^2 \sim 9 \times 10^4$ T^2 m^{-1}) could be generated.[44] They measured the magnetophoretic velocities of individual emulsion droplets and determined the extraction ratio of an Mn(II)–TTA complex[44] and the interfacial concentration of Dy(III) alkylcarboxylate.[45,46] The detection limit of Mn(II) attained the attomole level. Further, Suwa and Watarai succeeded in measuring the rapid photo-induced spin transition of a single crystal of cobalt–iron polycyanide[47,48] from the change in the magnetophoretic velocity just after the irradiation of a pulse laser light of 532 nm.[49,50] Egami and Watarai[51] showed the usefulness of a magnetic circuit, which was an assembly of permanent magnets and could generate a strong magnetic field (max. 2.8 T) and a gradient (max. $\nabla B^2 = 7.8 \times 10^3$ T^2 m^{-1}). They could measure the interfacial magnetic susceptibility and interfacial concentration of Prussian blue on a single toluene droplet. The magnetophoresis of a single microbubble in an organic liquid was measured together with laser-thermophoresis.[52] The bubble behaved like a paramagnetic particle in a diamagnetic organic liquid, and the magnetophoretic velocity of the bubble was used to estimate the magnetic susceptibility of the organic liquid. Their works indicated that the magnetophoretic velocity analysis is a potential tool for the basic study of microscale chemistry and materials science.

Recently, Watarai and Chen[53] showed the feasibility of the mole-ratio method utilizing magnetophoretic velocimetry. The mole-ratio method has been widely used to determine the composition of metal complexes, commonly utilizing spectroscopic measurement. The diamagnetic C-18 silica particles adsorbed with a hydrophobic phosphate ligand (L) were dispersed in an aqueous solution of a paramagnetic metal ion (M), whose concentration was not very high to affect χ_m. The metal complex (ML_q) was formed on the hydrophobic pore surface of the silica particle, and thus χ_p increased. Fig. 3B shows the plots of the normalized velocity of v_{mag}, which was obtained as the ratio of the magnetophoretic velocity to the maximum velocity at the fixed magnetic field gradient position, against the mole-ratio of the metal to ligand. Similar to the traditional mole-ratio method, the plots were approximated by two straight lines, and the intersection of these lines corresponded to $1/q$. The device of this method is simple and inexpensive, as shown in Fig. 3A. This method was also applied to micro-solvent extraction systems.[54] The magnetic mole-ratio method can detect picomoles of paramagnetic ions and is especially advantageous for systems with no characteristic absorption bands.

The measurement of the magnetophoretic velocity of sub-micrometer-sized fluorescent polystyrene spheres was demonstrated in 0.5 M $MnCl_2$ aqueous solution.[55] Given that it was hard to directly measure their diameter (0.5–5 μm) with an optical microscope, the size of the particles was estimated from the Brownian motion perpendicular to the field gradient. Watarai *et al.* also proposed an alternative way to avoid the problem of the size measurement in

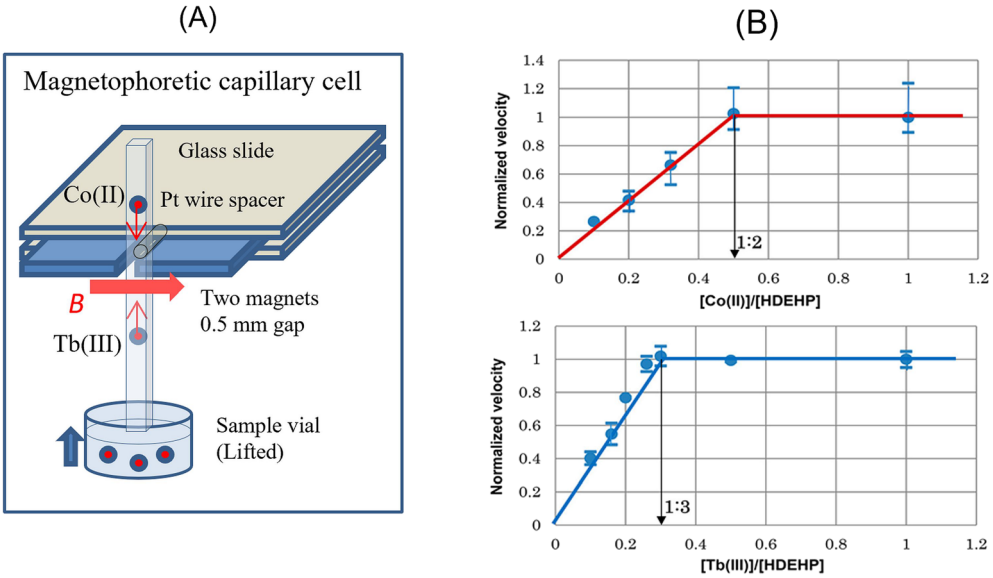

Fig. 3 (A) Schematic drawing of the cell to measure the magnetophoretic velocity of a C18-silica particle adsorbed by a metal complex with bis(2-ethylhexyl)hydrogen phosphate (HDEHP). (B) Magnetophoretic mole-ratio plots determining $Co(DEHP)_2$ and $Tb(DEHP)_3$. Reprinted with permission from ref. 53. Copyright © 2017, the American Chemical Society.

magnetophoretic velocity analysis, which is regarded as zero-velocity magnetophoresis.[56] The magnetophoretic velocity of a particle in a liquid medium must be zero at $\chi_p = \chi_m$ when the influence of gravity force is removed. In this feasibility study, the χ_m of the aqueous medium was varied by adding $DyCl_3$, or the χ_m of the nonaqueous medium was changed by using different organic solvents. The magnetophoretic velocity normalized by ∇B^2 against χ_m had a linear relationship, and the extrapolation of χ_m to $v_{mag} = 0$ yielded χ_p. This method not only can be applied to smaller particles but also to non-spherical particles or the measurement of the magnetic susceptibility of the medium.

2.1.2 Magnetophoresis of magnetic particles. Magnetic beads are widely used as a label for the separation of biological cells. The magnetic beads typically contain superparamagnetic iron oxide magnetic nanoparticles (MNPs). In a sufficiently high magnetic field (>0.1 T), the magnetization reaches saturation M_s. In this condition, the effective magnetic moment can be expressed by $m_{eff} = M_s V$, the direction of which is parallel to the external magnetic field. Therefore, as the magnetic moment becomes constant, ∇B is a better parameter for the magnetophoresis of MNPs than ∇B^2.

It is of great interest how small MNPs are moved by a magnetic force. Lim *et al.*[57] studied the magnetophoretic behavior of individual iron oxide MNPs (38 nm magnetic core and a 67 nm thick polymer/Au nanoparticle plasmonic shell) using a dark-field optical microscope. The magnetic field gradient of 100–1000 T m^{-1} was produced by an electromagnet and a thin (5 μm) pole piece of mu-metal as a magnetic tweezer. They observed the magnetophoretic displacement of an iron oxide MNP located at a distance of less than 10 μm under a magnetic field gradient, which was sufficient to dominate the Brownian motion. Zhang *et al.*[58] also measured the magnetophoretic velocities of single MNPs in a microchip with a permanent magnet, which were found to be 2.73 μm s^{-1} for 160 nm diameter MNPs and 23.6 μm s^{-1} for diameter 500 nm MNP. Their studies suggested that this type of larger single MNP can be moved by an Nd–Fe–B magnet, and the migration velocity of MNPs can be utilized for viscoelastic force measurements in living cells.

MNPs were used for solid-phase extraction because they are easily collected with a permanent magnet from a sample solution. However, in this type of system, MNPs tend to form complex aggregates and agglomerates. Therefore, the separation behavior cannot be explained by the magnetophoresis of simple individual MNPs. According to the fundamental studies by Lim *et al.*,[59] to account for the separation with weak magnetic field gradients, two physical effects should be considered, *i.e.*, cooperative magnetophoresis and magnetophoresis-induced convection. The former means the magnetophoresis of strongly interactive particles or chain-like aggregates formed by dipole–dipole interaction induced by a magnetic field.[60] The aggregation of MNPs dramatically enhances the magnetophoretic velocity.[61] Alternatively, the latter indicates a fluid dynamic instability due to an inhomogeneous magnetic field.[62] As depicted in Fig. 4A and B, the magnetic force near the magnet is stronger than far from it. Therefore, the inhomogeneous motion of MNPs causes convection in a cuvette by momentum transfer between MNPs and the surrounding fluid, as shown in Fig. 4C. This convective motion boosts the magnetophoretic capture of MNPs. Their study provides insights into the design of MNPs and magnetic separation systems.

2.2 Magnetic manipulation of micro/nano particles

2.2.1 Levitation and trapping of diamagnetic particles in paramagnetic media. Microparticles can be magnetically levitated under a magnetic field gradient. Magnetic levitation can be performed at the vertical position z, where the magnetic force balances with the gravity force, as follows: $(\chi_p - \chi_m)(B\partial B/\partial z)/\mu_0 - (\rho_p - \rho_m)g = 0$. The condition $\chi_p < \chi_m$ is needed for stable levitation when $\rho_p > \rho_m$ and $(B\partial B/\partial z) < 0$. In this condition, a repulsive force acts on the particles from the magnetic attraction of the medium. This force is called "magnetophoretic buoyancy". Ikezoe *et al.*[63] demonstrated the levitation of water ($\chi_p = -9.03 \times 10^{-6}$, a volume of ~7 cm^3) in oxygen gas ($\chi_m = 1.80 \times 10^{-6}$, 12 atm) under an inhomogeneous magnetic field generated by a superconducting magnet (B = 10 T, $|B\partial B/\partial z|$ = 420 T^2 m^{-1}). If the medium is air ($\chi_m = 0.38 \times 10^{-6}$), $|B\partial B/\partial z| > 1400$ T^2 m^{-1} is required for the levitation of water. Based on this enhancement of the magnetic force in oxygen, they utilized magnetic levitation to separate KCl and NaCl powders.[64] Glass particles, whose density and magnetic susceptibility are not the same, are suspended in 6.0 wt% $MnCl_2$ aqueous solution and well separated to different equilibrium positions.[64]

Instead of gravity, Namba and Watarai combined the vertical flow of the medium with magnetic buoyancy to trap a particle depending on the size and magnetic susceptibility.[65] They demonstrated the magnetic trapping of human blood cells suspended in 0.1 M $MnCl_2$ aqueous solution under a gradient of 1800 T^2 m^{-1} generated by permanent magnets in a square capillary tube (100 μm × 100 μm in the inner section). The blood cells could be trapped at the edge of the pole pieces, and complete trapping could be performed when the flow rate was less than 1 μL h^{-1} (~30 μm s^{-1}).

Whitesides and colleagues have developed an analytical separation technique that utilizes the levitation principle (called "MagLev").[66] They made a minimal point of B^2 between a pair of permanent magnets with a like-pole-facing configuration (N–N or S–S). After putting a powder sample in a paramagnetic liquid (for example, $MnCl_2$ or Gd(III) complex aqueous solution) between the magnets, the sample started moving to the equilibrium position, which depended on its density and magnetic susceptibility. They especially focused on the difference in density as a characteristic parameter for separation rather than magnetic susceptibility. This method has comprehensive applicability with various diamagnetic samples, such as polymers,[67] foods,[68] crystal polymorphs,[69] and illicit drugs.[70]

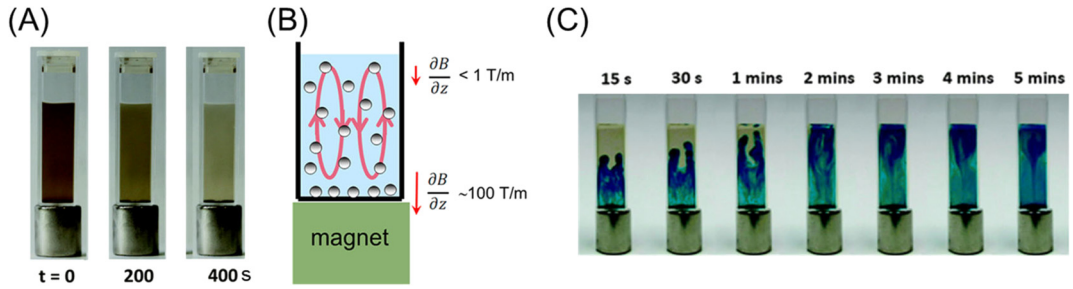

Fig. 4 (A) Time-lapse images of the capture of MNPs (*ca.* 30 nm) in diluted suspension with a permanent magnet. (B) Illustration of the convection induced in a MNP suspension by an inhomogeneous magnetic field. (C) Time-lapse images of macroscopic convection visualized using a dye (methylene blue). Reproduced from ref. 62 with permission from The Royal Society of Chemistry.

Using magnetophoretic buoyancy, Rodríguez-Villarreal *et al.*[71] demonstrated the continuous focusing of diamagnetic particles in a capillary flow system. The capillary cell was placed at the gap (300 μm) between two Nd–Fe–B permanent magnets with a like-pole-facing configuration. The suspension of diamagnetic particles in a paramagnetic aqueous solution flowed in the capillary. The diamagnetic particles were repelled from both magnets and continuously focused on the center of the capillary. They examined different types of particles (polystyrene microspheres and HaCaT cells) and paramagnetic solutions ($MnCl_2$, $GdCl_3$, and gadolinium(III)-diethylenetriaminepentaacetic acid (DTPA)).

Graphite is strongly diamagnetic and has magnetic anisotropy. For highly oriented pyrolytic graphite (HOPG), the magnetic susceptibility along its out-of-plane direction (perpendicular to the graphene plane) is -5.82×10^{-4}, whereas that along the in-plane direction is -8.2×10^{-5}. Given that the magnetic susceptibility of water is -9.0×10^{-6}, the magnetophoretic buoyancy could be subjected to HOPG in water. Nguyen *et al.*[72] investigated the magnetophoretic behavior of a HOPG flask with full sizes of 4.6 μm × 3.4 μm × 1.2 μm on average. A pair of permanent magnets produced the magnetic field (>1 T) and the field gradient of ∇B^2 = 2300 T^2 m^{-1}, which was strong enough to align the HOPG flask with the graphene planes parallel to the magnetic field. They successfully measured the magnetophoretic velocity of lipid-coated graphite in NaCl aqueous solution, suggesting a way for previously undiscovered biomedical applications.

Dunne *et al.*[73] reported an interesting attempt to make a microfluidic channel in a magnetic fluid by utilizing magnetic buoyancy. They fabricated a quadrupolar magnet consisting of four bar magnets, as shown in Fig. 5. A null magnetic field at the center of the quadrupolar magnet was created. Diamagnetic water in ferrofluid was confined at the null magnetic line, and then a "water antitube" was formed. This liquid-in-liquid channel showed remarkable advantages including self-healing, non-clogging, near-frictionless, and adjustable thickness. A blanched antitube can be created by shaping two stacked magnets with waterjet-cutting. For example, the Y-junction of the antitube was successfully formed in ferrofluid. Furthermore, flow control, such as pumping and valving, in the antitube could be done by manipulating the field.

2.2.2 Magnetic manipulation and separation of microparticles in microfluidic devices. The combination of magnetic force and a microfluidic device enables the precise and complicated manipulation and separation of microparticles. Various ideas that utilize magnetic

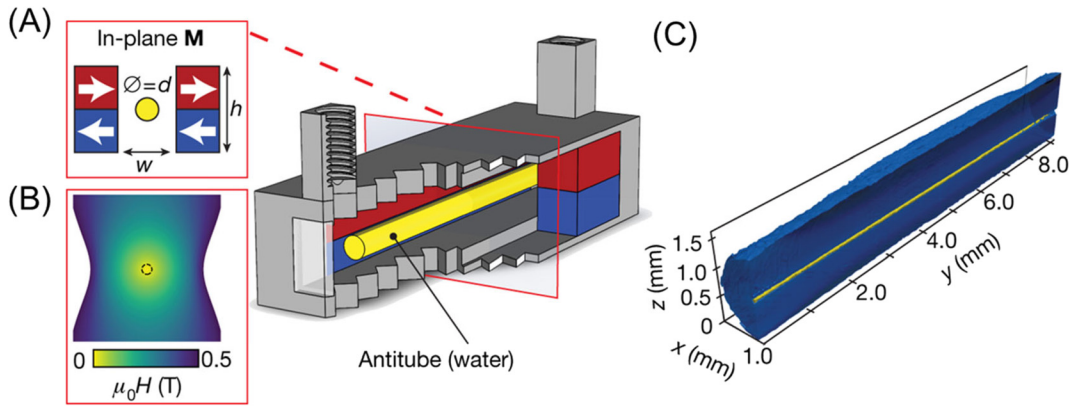

Fig. 5 (A) Permanent magnets (red, blue) in an in-plane quadrupolar configuration. The yellow area shows a low-field zone created at the centre, where an antitube of water is stabilized inside an immiscible magnetic liquid. (B) Contour plot of the magnetic field. (C) Synchrotron X-ray tomographic reconstruction of a water antitube (yellow) with a diameter of 81 μm, surrounded by ferrofluid (blue). Reproduced from ref. 73 with permission. Copyright © 2020, Springer Nature.

manipulation have been proposed in the field of lab-on-a-chip[74–79] after the work of Pamme *et al.*[80] They fabricated a microchip with a 6 mm × 6 mm separating chamber, 16 buffer inlets, 1 sample inlet, and 17 outlets, causing the flow speed in the chamber to become uniform.[80] A magnetic field gradient was applied perpendicular to the flow direction. They successfully separated particles based on the difference in deflection. Recently, the deflection in the continuous flow was utilized to fabricate polyelectrolyte (PE) microcapsules for drug delivery. As shown in Fig. 6A,[81] the ferrofluid droplet was deflected through a multilayer stream by magnetic force. They successfully produced multilayer PE-coated capsules in 1 step.

Navi *et al.*[82] fabricated a continuous cell separation platform using an aqueous two-phase system (ATPS), which consisted of a dextran (DEX)-rich lower phase and polyethylene glycol–polypropylene glycol–polyethylene glycol (PEG–PPG–PEG) triblock copolymer-rich upper phase. As shown in Fig. 6B, the microchip was filled with ferrofluid in the PEG–PPG–PEG phase, whereas the cell suspension in the DEX phase was injected through a microneedle. Due to the cell-triggered Rayleigh–Plateau instability, the cell-encapsulated droplets were larger than the empty droplets. Then, the difference in magnetic buoyancy on these droplets resulted in distinguishable deflection in the microchip. This technique does not require a cumbersome procedure of magnetic labeling.

Zhang *et al.*[83] demonstrated comprehensive two-dimensional manipulation of diamagnetic microdroplets in ferrofluid by hydrostatic pressure and magnetophoretic buoyancy. Fig. 6C summarizes the concept of manipulation. A diamagnetic oil droplet is individually generated at a T-junction by controlling the hydrostatic pressure of the ferrofluid and the oil. The droplet is transported to the microwell array region by the ferrofluid flow. The motion of a droplet can be controlled in the $\pm X$-direction and $\pm Y$-direction by hydrostatic pressure and magnetophoretic buoyancy, respectively (Fig. 6C). They demonstrated the trapping of a droplet in a preferred microwell, exchange of the droplet positions, and contact and fusion of the droplets. This manipulation strategy can perform four essential steps in chemical experiments including sampling, dilution, reaction, and detection.

Complex microfluidic devices that combine a magnetic field with other external fields were fabricated to achieve precise cell sorting. A rare cell (such as circulating tumor cells, CTCs) sorting method, which combined acoustic field, flow field and magnetic field, was demonstrated.[84] As shown in Fig. 6D, on-chip analysis of individual cells was carried out using a microchip composed of three zones: as follows: (1) the focusing zone by acoustic standing wave, (2) separation zone by the combination of flow and magnetic field, and (3) capturing zone by microwell array with micro-magnets. As a demonstration, a small amount of adherent human prostate cancer (LNCaP), which served as surrogates for CTC, was spiked in a suspension of leukocytes, followed by selective magnetic labeling to LNCaP. The initial ratio of LNCaP to leukocytes was ~1 : 150. After passing the magnetic separation zone of this microchip, the LNCaP cells were enriched over 100-fold. Further, the microwell array could

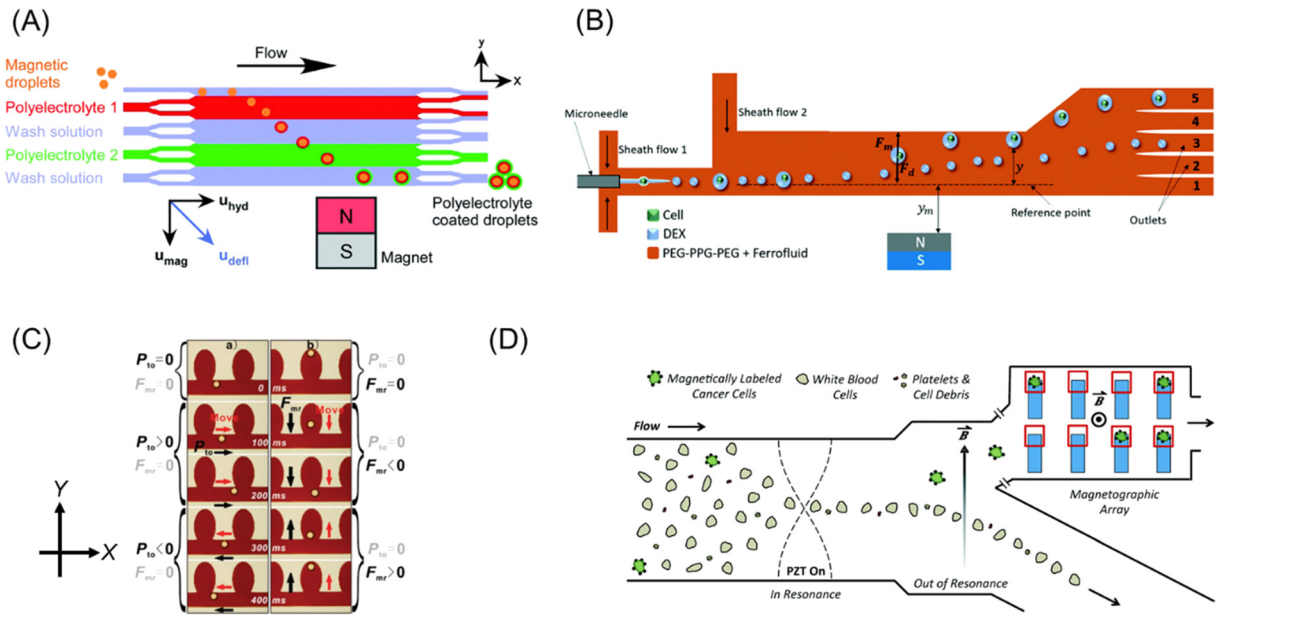

Fig. 6 (A) Concept of continuous flow particle coating and washing *via* the deflection of magnetic templates through multi-laminar flow streams of polyelectrolyte and washing solutions. Reproduced from ref. 81 with permission from the Royal Society of Chemistry. (B) Schematic illustration of the selective separation of cell-containing droplets utilizing ATPS. Reproduced from ref. 82 with permission from The Royal Society of Chemistry. (C) Microscopic images of droplet motion in microstructures. Black and red arrows indicate the direction of the applied forces and droplet motion. Reprinted with permission from ref. 83. Copyright © 2011, the American Chemical Society. (D) Illustration of microfluidic system for the separation of rare cells, which uses acoustic and magnetic fields. Reproduced from ref. 84 with permission from The Royal Society of Chemistry.

capture the magnetically labeled cancer cells with an accuracy exceeding 80%. Thus, this system is promising for liquid biopsies, single-cell biology, and immunology.

Digital microfluidics (DMF) is liquid-handling technology that manipulates liquids in discrete droplets in integrated microfluidic devices, usually by the force of an electric field gradient.[85] In the case of a ferrofluidic droplet, a magnetic force was employed to actuate the droplet by moving a magnet under the flat substrate.[86] Wheeler's group demonstrated the flexibility of DMF by combining biosensor-based electrochemical measurement of glucose with a chemiluminescent magnetic bead-based sandwich immunoassay for insulin.[87] In direct blood loading for plasma separation and diagnostic assays by paramagnetic particle DMF, they demonstrated a 21-step rubella virus (RV) IgG immunoassay, yielding a detection limit of 1.9 IU mL^{-1}, below the diagnostic cut-off.[88] Further, they demonstrated portable sample-processing DMF molecular assays for the detection of the Zika virus from a 5 μL sample using RNA captured on magnetic beads.[89]

Oleschuk's group showed that the combination of low-friction superhydrophobic surfaces and droplets containing superparamagnetic particles could reliably dispense droplets with high precision (≤6%). Droplets ranging in size from 5 to 20 μL were used for an EDTA-based on-chip complexometric colorimetric titration for water hardness.[90] Furthermore, precise control of droplets in magnetically driven DMF platforms was achieved using a low-friction surface, magnetically susceptible material/droplet(s), and an applied magnetic field. The optimized platforms were applied in a quantitative fluorescence-based DNA assay under 2 min.[91]

2.3 Magnetic force and chemical interaction

2.3.1 Dynamic force measurements. The force measurement of a single chemical interaction succeeded for DNA by applying a pulling force using a magnetic bead in 1992 by Finzi *et al.*[92] Individual λ-DNA (48.5 kbp) molecules were chemically attached by one of their ends to a glass slide and by their other end to a magnetic bead of 2.9 μm in diameter. In a flow device, they measured the extension *versus* force curves for individual DNA molecules at three different salt concentrations with forces in the range of 10^{-14} to 10^{-11} N. Intercalation of ethidium bromide did not change the elasticity of the molecule but elongated about 40% of its maximum length. Strick *et al.* used a magnetic field to rotate the beads, and thus coil and pull a single DNA in a closed device. They used the Brownian fluctuations of a DNA-tethered bead to measure the vertical stretching force working on the molecule. They investigated the elastic behavior of individual λ-DNA molecules over- and underwound by up to 500 turns.[93] A sharp transition was discovered from a low to a high extension state at about 0.45 pN for underwound molecules and at a force of about 3 pN for the overwound molecules, reflecting the probable formation of alternative structures in stretched coiled DNA molecules. After these works, the design and optimization of magnetic tweezers of a single DNA were investigated.[94] The advantages of magnetic tweezers for micromanipulation have been comprehensively reviewed against the cantilever method and optical tweezers.[95] Straightforward control of the supercoiled state of DNA, facile extension to the parallel measurement of multiple molecules, integration with fluorescence measurements, and the simplicity and robustness of the experimental configuration were emphasized as the advantages of magnetic tweezers in a book chapter.[96] Recently, from single-molecule thermodynamic measurements of double-stranded DNA by magnetic tweezer experiments under controlled temperatures, the first simultaneous determination of the entropy (ΔS) and enthalpy changes (ΔH) of the structural transitions of DNA was reported, where for the hysteretic peeling transition, $\Delta S \sim 20$ cal K^{-1} mol^{-1} and $\Delta H \sim 7$ kcal mol^{-1} and for the non-hysteretic transition, $\Delta S \sim -3$ cal K^{-1} mol^{-1} and $\Delta H \sim 1$ kcal mol^{-1} were determined.[97] To determine how CpG methylation affects DNA condensation, the equilibrium hopping dynamics between the condensed and extended states of DNA was studied by magnetic tweezers using a magnetic bead-RNA–DNA–RNA-cover glass structure in the presence of 3+ or 4+ ions as a reduced model of histone tail DNA (Fig. 7).[98] CpG methylation of each cytosine nucleotide substantially increased the DNA–DNA attraction by up to $0.2k_BT$. For the DNA with 57% GC content, the relative increase caused by CpG methylation was up to 32% for the spermine(4+)-induced DNA–DNA attraction and up to 9% for the polylysine(6+)-induced DNA–DNA attraction.

Applying an external pulling force to individual molecules can change their equilibrium structure and dissociate their bonds in some cases, as reported in the studies of dynamic force spectroscopy, though major subjects of magnetic tweezers were DNA.[99–101] Cysteamine molecules were tethered to Ag nanoparticles on a glass slide with SH end and to magnetic beads with NH_2 end forming an amide group. With an increase in the pulling force from 0 to 100 pN per magnetic bead, the surface-enhanced Raman scattering (SERS) intensity ratio of ν(C–S) *trans*/ν(C–S) *gauche*, corresponding to the equilibrium isomer ratio of cysteamine, increased from 0.6 to 1.08, indicating an increase in the *trans* form from 37% to 52%.[102] This result suggested that the *trans* form, which has a longer molecular structure than the *gauche* form, is stabilized under the pulled condition. A quartz crystal microbalance (QCM) is known as an extremely sensitive device for the measurement of very small weight changes in the order of ng. Yu *et al.* fabricated a conductive polyaniline-coated QCM and detected the weight increase due to the HCl vapor absorption when a magnetic field (0–3.1 T) was applied.[103] Imai and Watarai prepared a QCM (9 MHz) electrode adsorbed with magnetic beads (200 nm in diameter, modified by poly-glycidyl methacrylate) on the Au electrode surface, forming a layered structure. Then, the interaction energy between the layers was measured by changing the environmental temperature under the

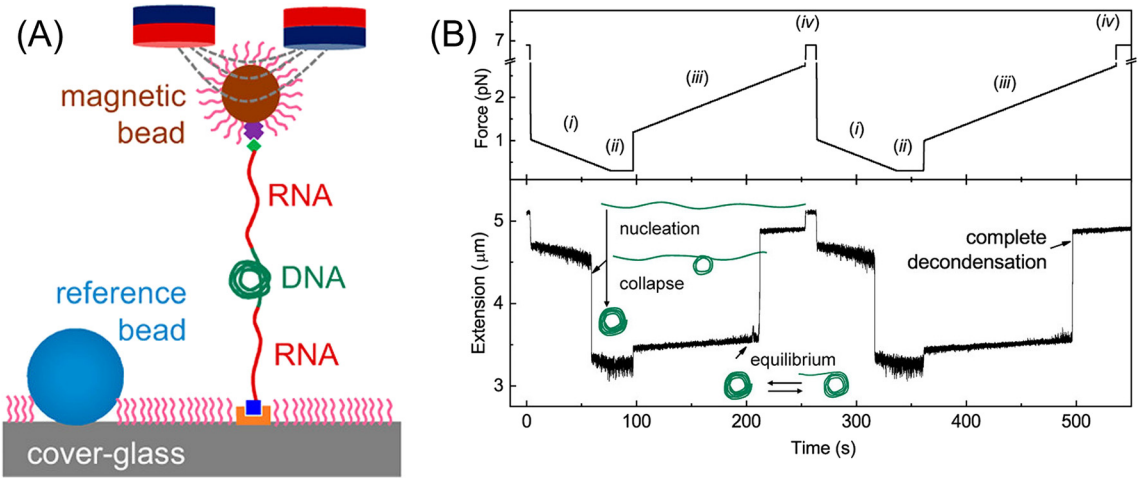

Fig. 7 (A) Setup of magnetic tweezers. (B) Time-extension course recorded during repeated force-cycles obtained at 0.2 mM $Co(NH_3)_6^{3+}$ using nonmethylated DNA: (i) force-decreasing region with −0.01 pN s^{-1}, leading to nucleation and condensation, (ii) low constant force is kept for 20 s, (iii) force-increasing region with 0.01 pN s^{-1}, where through equilibrium state DNA completely decondensed, and (iv) high constant force is kept for 10 s. Reprinted with permission from ref. 98. Copyright © 2020, the American Chemical Society.

application of pulling force by a magnetic circuit (3.5 T). The desorption rate of magnetic beads under a high magnetic field gradient was measured from the frequency shift of the QCM. The activation energy of 21 kJ mol^{-1} was obtained, corresponding to the hydrogen bonding enthalpy (10–30 kJ mol^{-1}) between the polar groups of S–H, N–H, and O–H on the surface of the magnetic beads.[104]

2.3.2 Magneto-capillary effect. The self-assembly of small substances on a liquid surface by attractive capillary force is known as the "Cheerios effect".[105] Vandewalle *et al.* reported that the equilibrium distances of two and three hydrophobic magnetic beads (500 μm in diameter) on the water surface could be controlled by the dipole–dipole magnetic repulsive force between the particles (*cf.* Fig. 1C) with a vertical magnetic field (up to 5 mT) applied to the surface.[106] The change in equilibrium distances between the beads due to the magnetic repulsion was theoretically interpreted. However, the detachment of a pair of beads once attached required a higher magnetic field (a larger detaching force) than that observed in the attachment process, suggesting that the attachment–detachment process is not a simple reversible process. The detachment process should require excess energy, similar to the "activation energy" in chemical kinetics. They further studied the ordering of particles for large assemblies and found an upper size limit above which the assembly collapses due to the curvature of the interface induced by the weight of the self-assembly.[107]

Bishop *et al.* demonstrated the rapid motion of a magnetic Janus particle (4 μm in diameter), composed of a hydrophobic polystyrene hemisphere and a hydrophilic magnetic hemisphere of 3-mercaptopropionic acid on 20 nm Au/25 nm Ni/5 nm Ti layers on the curved liquid–liquid interface of a water droplet (291 μm in radius) in decane.[108] The application of a static homogeneous vertical field of 15 mT drove particle motion to the drop equator, where the particle magnetic moment could align parallel to the field

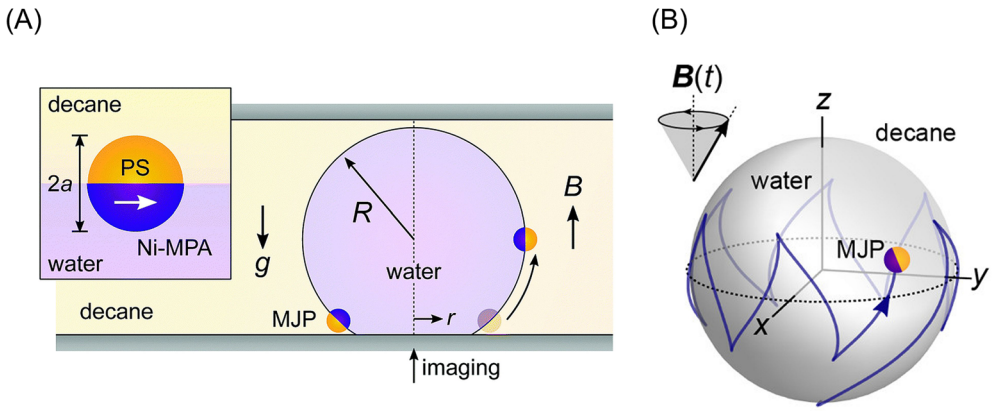

Fig. 8 (A) Schematic illustration of a magnetic Janus particle (MJP) moving on the curved interface of a water droplet in decane due to a homogeneous magnetic field *B*. The inset shows the preferred orientation of the MJP at the interface and its magnetic moment (white arrow). Reproduced from ref. 108 with permission from The Royal Society of Chemistry. (B) Simulation of zig-zag motion of MJP in the interface due to a precessing magnetic field. Reprinted with permission from ref. 110. Copyright © 2020, the American Chemical Society.

(Fig. 8A). Furthermore, they demonstrated that time-varying (spatially uniform) magnetic fields could drive a variety of steady particle motions on the interface of a water droplet in decane. Upon the application of a precessing field, the magnetic Janus particles moved either along circular orbits at the drop poles or along zigzag paths at the drop equator (Fig. 8B). They suggested that the observed magneto-capillary particle motions can be used to enhance the mass transfer in emulsions stabilized by magnetic particles.[109]

2.4 Application of magnetic force to separation methods

Solid-phase extraction (SPE) and liquid–liquid extraction (LLE) are fundamental separation techniques in analytical chemistry. However, traditional extraction methods require organic solvents or solid adsorbate, which are often not eco-friendly. Thus, to solve this problem, many attempts to impart magnetism to the extraction media have recently been reported.

The extraction particles in SPE are commonly packed in cartridges and used with high performance because a large specific area is preferable for the rapid adsorption of the analytes. Recently, surface-modified MNPs have been recognized as potential materials for SPE because they can be collected with a magnetic field in a non-contact manner from a dispersed mixture with the sample solution. Also, it can be functionalized with various molecules to offer high selectivity of a target analyte. There have been many reports on the use of magnetic beads in SPE for a wide variety of analytes.[111–118]

Further, it is possible to decorate MNPs with a layer of metal–organic frameworks (MOFs) for use in SPE. MOFs are porous polymeric materials composed of metal ions as cross-linking points and organic ligands as bridges. The analytes are adsorbed in the pores due to hydrophobic interactions, π–π stacking with aromatic rings in ligands, hydrogen bonding, ionic interactions, dipole–dipole interactions, and Lewis acid–base interactions with uncoordinated sites of linking metals. Hence, MOFs can have excellent molecular selectivity and absorption capacity, and their combination with MNP enables the separation and enrichment of low-abundant species, such as toxic metal ions in water,[119–122] peptides in body fluids,[123,124] and dyes from contaminated water.[125,126] Recently, the enrichment of exosomes,[127] which is promising as a biomarker for cancer, in a urine sample was performed with a Zr-MOF-functionalized MNP. Exosomes specifically adsorbed on the pores of this magnetic MOF due to the bond between the Zr–O unit and the phospholipid bilayer, and then magnetically separated from the complex biological fluid. They achieved a high recovery rate of exosomes (>95%) with 10 min incubation.

Ionic liquids (ILs),[128] which are room-temperature molten salts, are a promising extraction solvent due to their low toxicity, low vapor pressure, and high thermal stability. Their physical and chemical properties, such as hydrophobicity, power to dissolve chemical and biological compounds, and viscosity, can be tuned by replacing their organic cations and/or organic/inorganic anions. Recently, magnetic property was added by using paramagnetic metal complex anions such as $FeCl_4^-$, $GdCl_6^{3-}$, and Ni(II) hexafluoroacetylacetonate.[128,129] These materials are called magnetic ionic liquid (MIL), which possess high magnetic susceptibility and can easily be recovered with a permanent magnet. Several research groups showed the potential of MILs as an extraction solvent for drugs,[130] environmental pollutants,[131] hormones,[132] bacteria,[133] *etc.* A notable application of MILs is DNA purification and preconcentration.[134–139] Traditionally, LLE is used for DNA isolation, but it needs a large amount of organic solvent, which causes the loss of the DNA. Further, the multiple centrifugation steps to remove cellular residue are time-consuming and a significant bottleneck in DNA analysis. Thus, to improve this situation, Wang *et al.*[135] studied DNA extraction in a hydrophobic MIL, which consisted of a hexaalkylguanidinium cation and paramagnetic metal complex anion (Fig. 9A). An aliquot (20 μL) of MIL was added in 1.0 mL aqueous solution of DNA, and then stirred by vortexing. The dispersed MIL, which extracted DNA, was gathered by applying a magnetic field (Fig. 9B). At a lower pH, satellite DNA (stDNA) was well extracted into the MIL phase, while proteins remained in the aqueous phase (Fig. 9C). Therefore, stDNA could be purified and enriched before PCR assay.

The effect of a magnetic field on solvent extraction equilibria has not been reported, but Tsukahara *et al.*[140] discovered the influence of magnetic force on the extraction rate of paramagnetic Eu^{3+} with 2-thenoyltrifluoroacetonate (tta^-) anion from oxalate (ox^-) solution to the dodecane phase. By microscopic observation of the dodecane/water interface sandwiched with permanent magnets, they observed random flashing spots due to the extraction of fluorescent $Eu(tta)_3$ in the dodecane side of the interface (Fig. 10A). Further, when the magnetic field gradient applied to the interface increased, the flash frequency increased (Fig. 10B). The mechanism of random flashing was thought to be the formation of micro-aggregates of non-fluorescent and paramagnetic $Eu(tta)(ox)^+$ complex in the aqueous phase, which migrated to the interface by magnetophoretic attraction and reacted with excess Htta in dodecane to form fluorescent $Eu(tta)_3$ at the interface[141] (Fig. 10C).

Fuh *et al.* developed analytical magnetapheresis and applied it to blood typing.[142] They also developed the magnetic thin channel method to trap and concentrate functional magnetic particles and used it for the immunological analysis of C-reactive protein,[143] hepatitis B surface antigen,[144] and tumor necrosis factor-α.[145,146]

Studies of the magnetic field effect on chromatography are limited. Mukherjee *et al.* reported in 1980 on the magneto-paper electrophoresis of inorganic ions using 1.5 T electromagnet.[147] They observed that the migration distance of trivalent lanthanide ions spotted on a 1 cm × 35 cm paper strip was retarded by a magnetic field, and the magnetic retardation effect was proportional to the effective magnetic moments of the ions. Nomizu *et al.* studied magnetic chromatography to separate a mixed suspension of hematite (0.2 μm φ × 1.0 μm long) and magnetite (*ca.* 0.6 μm in

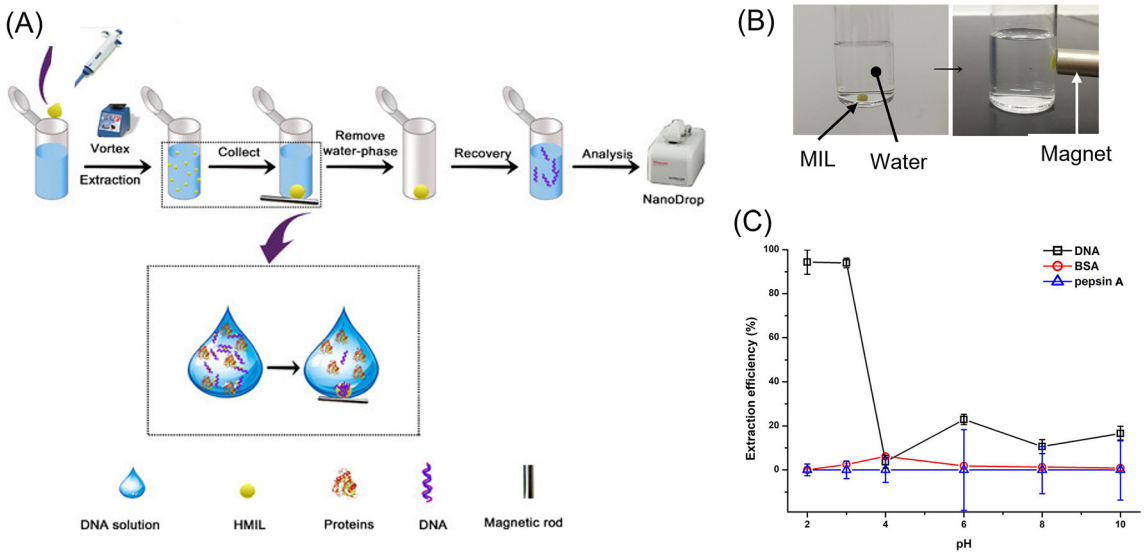

Fig. 9 Scheme of the extraction procedure (A), attractive behavior of an MIL droplet in water to a magnet (B), and extraction efficiency of stDNA, BSA, and pepsin A as a function of pH (C) for demonstration of the performance of the DNA extraction from complex samples. Reprinted with permission from ref. 135. Copyright © 2021, the American Chemical Society.

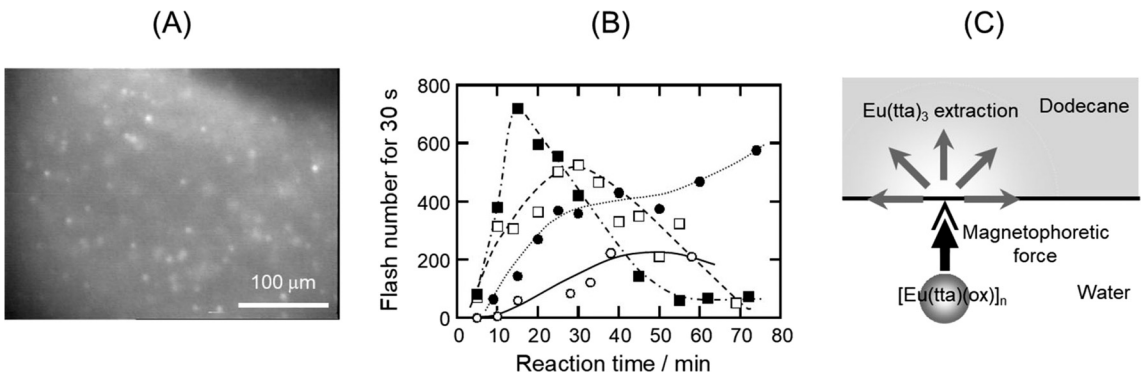

Fig. 10 (A) Random fluorescent flashing at the dodecane/water interface, showing the extraction of $Eu(tta)_3$. (B) Increase in the extraction rate of $Eu(tta)_3$ with a magnetic field; ○ no magnets, ● 2 magnets, □ 6 magnets, and ■ 8 magnets. (C) Illustration of the magnetophoresis of the micro-aggregates of $[Eu(tta)(ox)^+]_n$. Reprinted from ref. 140.

diameter) particles in a PTFE tube (1.5 mm o.d. × 0.5 mm i.d.) and successfully separated them by controlling the magnetic field application time.[148] Fujiwara *et al.* studied the migration of metal ions on silica gel under a magnetic field gradient of 410 T^2 m^{-1} and observed that their mobilities depended on the magnetic susceptibilities.[149,150] In the case of Cu^{2+}, they thought that the Cu^{2+} ions moved in a large group of Cu^{2+} ions and H_2O molecules with a diameter of 4.6 μm, not in a single Cu^{2+} ion.[151] Barrado and Rodríguez reported "high-performance liquid magneto-chromatography" in 2006.[152] They stated that its distinctive features are (a) a stationary phase with a high specific surface area of fine Fe_3O_4 particles supported on silica gel and (b) a variable intensity magnetic field with 0–5.5 mT. The effect of magnetic field on the retention time of amino acid after forming a Cu(II) complex was observed, but the separation performance was less than expected. Thus, fundamental studies on the packing materials and design of a magnetic field are required.

2.5 Micro-composites and magnetic force

Magnetic force can be used to arrange or organize microparticles in 2D or 3D structures, depending on their magnetic properties. They can sometimes exhibit unique properties, as found in photonic crystals. Also, magnetic force can actuate micro-subjects that were designed to generate expected mechanical motion. This section reviews some works relating to magnetic photonic crystals and magnetic soft robots, given that they will suggest valuable hints for analytical applications.

2.5.1 Magnetic photonic crystal. Two-dimensional photonic crystal (2D-PC) materials have attracted potential as chemical and biomolecular sensors, as reviewed by Asher *et al.*[153] The most widely used material for 2D-PC sensors is nonmagnetic polystyrene particles that are smaller than 1000 nm in diameter. Magnetic particles can also be arranged periodically in 1D, 2D, or 3D by combining the different

forces of magnetic dipole interaction and electrostatic interaction among particles. When the size of the magnetic particles matches the wavelength of visible or NIR light, a color change can be observed by applying an external magnetic field due to the change in distance among the periodically arranged particles. The recent development of magnetic photonic crystals was reviewed by Chen *et al.*[154]

A typical example of magnetic photonic crystals was reported by Yin *et al.* in 2007.[155] They prepared polyacrylate-capped superparamagnetic magnetite nanoparticles with diameters ranging from 30 to 180 nm *via* a high-temperature hydrolysis method. The diffraction color of a dispersion of these particles (120 nm in diameter) in water changed drastically from red to blue by the application of an external magnetic field in the range of 8.78 to 35.2 mT, where the diffraction peak shifted from 740 nm to below 450 nm, as shown in Fig. 11A. The application of magnetic photonic crystals to a humidity sensor has been reported by Ge *et al.*[156] They fabricated a thin film containing superparamagnetic Fe_3O_4@SiO_2 colloids (97 nm in core diameter) and a liquid precursor of poly(ethylene glycol) acrylate on an Nd–Fe–B magnet, followed by instant polymerization with UV-curable resin (NOA61) to fix the photonic structures formed through the magnetic assembly. The composite film contained hygroscopic poly(ethylene glycol) methacrylate (PEGMA) and crosslinker poly(ethylene glycol) diacrylate (PEGDA), which can strongly absorb water vapor, and therefore swelled upon contact with humid air, which led to visual color changes due to the increase or decrease in the lattice constant of the fixed ordered photonic structure (Fig. 11B). By optimizing the cross-linking level and the thickness of the polymer film, the reflection wavelength of the humidity sensor shifted by 160 nm within several minutes. Its intensity was readable with the naked eye. In addition, the photonic humidity sensor showed good reversibility and durability. Other applications including magnetically responsive photonic watermarks on banknotes,[157] magnetically switchable plasmonic nanorods,[158] and magnetically aligned layer-by-layer assembly for noble optical materials[159] were reported. However, to date, the application of magnetic photonic crystals to micro-analytical systems has not been reported. A future trial concerning this subject is anticipated.

2.5.2 Magnetic soft robots. Micro-scaled functional architectures that can be manipulated by a magnetic force have been reviewed under the name of "magnetic soft robots".[160] For example, a drug or cell-loaded porous magnetic hydrogel was fabricated and used for the controlled release and delivery of drugs or cells by magnetic field-induced deformation, respectively.[161] Magnetic soft capsules based on micro-assembled hard-magnetic composites rolled under weak rotating magnetic fields and squeezed themselves under a strong magnetic field to release the liquid drugs kept inside.[162] Self-propelled micromotors were fabricated by combining single-walled carbon nanotubes decorated by Fe_2O_3 nanoparticles on the outer surface and MnO_2 on the inner surface, which worked as catalysts for the reaction between H_2O_2 and phenylenediamine producing oxygen bubbles and colored substances depending on the isomers of phenylenediamine. The colored substance could be detected by the naked eye, and the magnetically trapped catalysts could be reused.[163] Magnetic active matters of

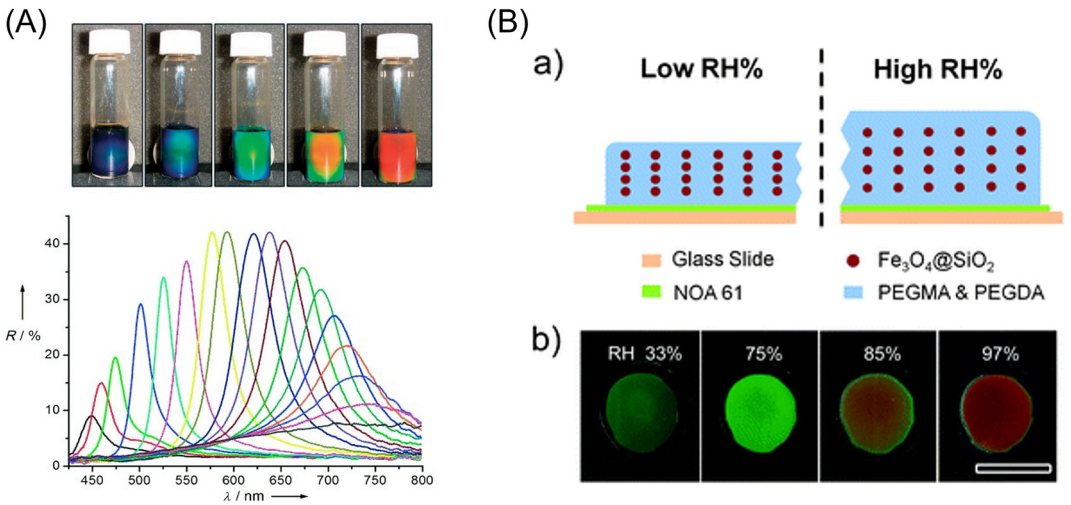

Fig. 11 (A) (Top) Photographs of colloidal crystals formed in response to an external magnetic field: the magnet–sample distance decreases gradually from right to left. (Bottom) Dependence of the reflection spectra at normal incidence of the colloidal crystals on the distance of the sample from the magnet. Diffraction peaks blue-shift (from right to left) as the distance decreases from 3.7 to 2.0 cm with a step size of 0.1 cm. Reprinted with permission from ref. 155. Copyright © 2007, WILEY-VCH Verlag GmbH & Co. KGaA, Weinheim. (B) (a) Schematic illustration of the structure of the humidity sensing film and the mechanism of color switching between low and high relative humidity (RH) environments. (b) Digital photos of a typical film with a 50% crosslink level in different humidity environments, showing blueish-green, green, yellow, and red. The scale bar is 1 cm. Reproduced from ref. 156 with permission from The Royal Society of Chemistry.

multifunctional swarming micro/nanorobots have been applied for *in vivo* medical use, such as the generation and locomotion of microswarms in bovine eyeballs,[164] overcoming restricted blood flowing in a porcine heart,[165] and whole-body-scale rapid delivery of cell collectives to the bile duct by combining endoscopy and microrobotic technology.[166,167] These ideas will stimulate the design of new principles for lab-on-a-chip analyses.

3. Application of magnetic torque

3.1 Orientation of diamagnetic substances under a dc magnetic field

Magnetic orientation occurs when a particle with magnetic anisotropy is exposed to an applied magnetic field (Fig. 1B). The magnetic anisotropy of a particle can be represented by the magnetic susceptibilities of χ_1, χ_2, and χ_3 (Fig. 13A). For simplification, a uniaxially anisotropic diamagnetic particle, where $\chi_1 > \chi_2 = \chi_3$, is considered. Under a static magnetic field, the magnetic torque on the particle can be expressed by

$$T = -\frac{B^2 V \Delta\chi}{2\mu_0} \sin 2\theta, \tag{11}$$

with the angle (θ) between the anisotropic axis, which is along χ_1, and the magnetic field, and $\Delta\chi = \chi_1 - \chi_2 = \chi_1 - \chi_3$. This equation indicates that the anisotropic χ_1 axis of the particle tends to align along the field direction, where $T = 0$ at $\theta = 0°$.

Generally, the magnetic susceptibility of a molecule is anisotropic. Taking benzene as an example, the magnetic susceptibility differs between the in-plane and out-of-plane directions of the aromatic ring, where the latter is more diamagnetic because of the induced ring current. Therefore, the benzene ring tends to align parallel to the field. Unfortunately, this diamagnetic anisotropic energy is negligibly smaller than the thermal energy of room temperature, and it is impossible to orient a single molecule with a magnetic field. When molecules form a μm-sized particle with ordered structure, such as aggregates and microcrystals, the magnetic energy becomes larger than the thermal energy.

Owing to the development of superconducting magnets in the 1990s, the magnetic orientation of various weak magnetic micrometer-sized objects can be observed. Higashi *et al.*[168,169] showed the magnetic orientation of red blood cells with their disk plane parallel to the magnetic field direction, and the dependence on the field strength up to 8 T suggested that their magnetic anisotropy was attributed to the molecular alignment of the lipid bilayer of cell membrane.[170] There are other reports on the magnetic orientation of diamagnetic micro/nano objects including porphyrin aggregates,[171,172] single-wall carbon nanotubes,[173] conducting polymer nanowires,[174,175] and gold nanorods.[176,177]

There are highly anisotropic diamagnetic particles, which can be aligned with an electromagnet or permanent magnet. For example, the needle-shaped monosodium urate (MSU) crystal has large magnetic anisotropy and can be oriented with a low magnetic field of 0.5 T.[178,179] MSU crystals develop in the joint and cause gout. Takeuchi *et al.*[180] reported a technique to detect MSU crystals by utilizing the magnetic orientation, aiming to develop a non-invasive diagnostic method for gout. They observed the angle distribution of the scattered near-infrared (NIR) light (785 nm) from a suspension of MSU needle crystals (12 μm in length, ~1 μm in width) induced by the application of a static magnetic field. Due to the magnetic orientation of the crystal, the angle distribution significantly changed.

Iwasaka and Mizukawa[181] showed the orientation of guanine crystals contained in fish scales under a weak magnetic field (<0.5 T). The guanine crystals were platy (20–30 μm in length, 5 μm in width, and 70 nm in thickness) and their planes oriented parallel to the magnetic field. The guanine crystal has a relatively high refractive index of 1.83, and thus it exhibits strong light reflection at the surface of the crystal.

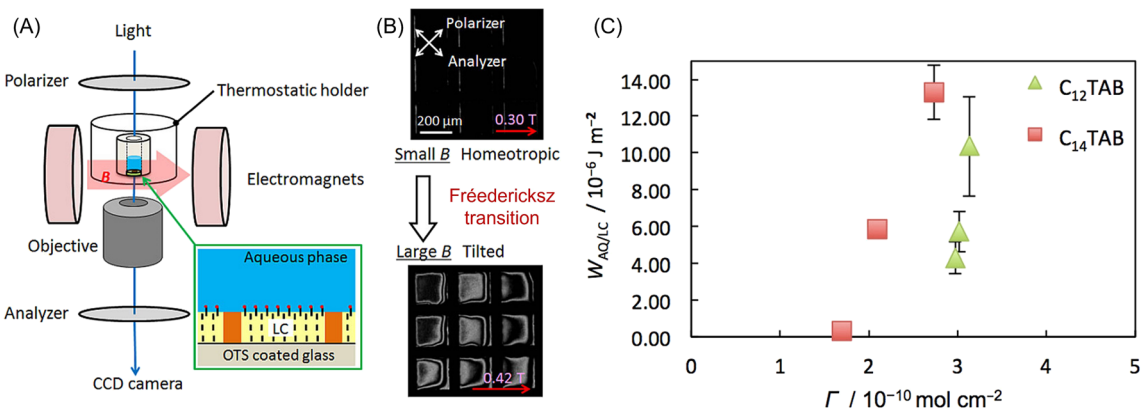

Fig. 12 (A) Experimental setup for the observation of the Fréedericksz transition of a LC thin layer in contact with an aqueous solution. LC thin layer (~20 μm) was supported by a Cu TEM grid and an octadecyl trichlorosilane (OTS)-coated glass, which induced homeotropic alignment. (B) Changes in polarized light microscope images with an increase in the magnetic field from 0.3 T to 0.42 T. (C) Plots of the anchoring energy ($W_{AQ/LC}$) against the surfactant concentration in the aqueous phase. Reprinted with permission from ref. 186. Copyright © 2018, the American Chemical Society.

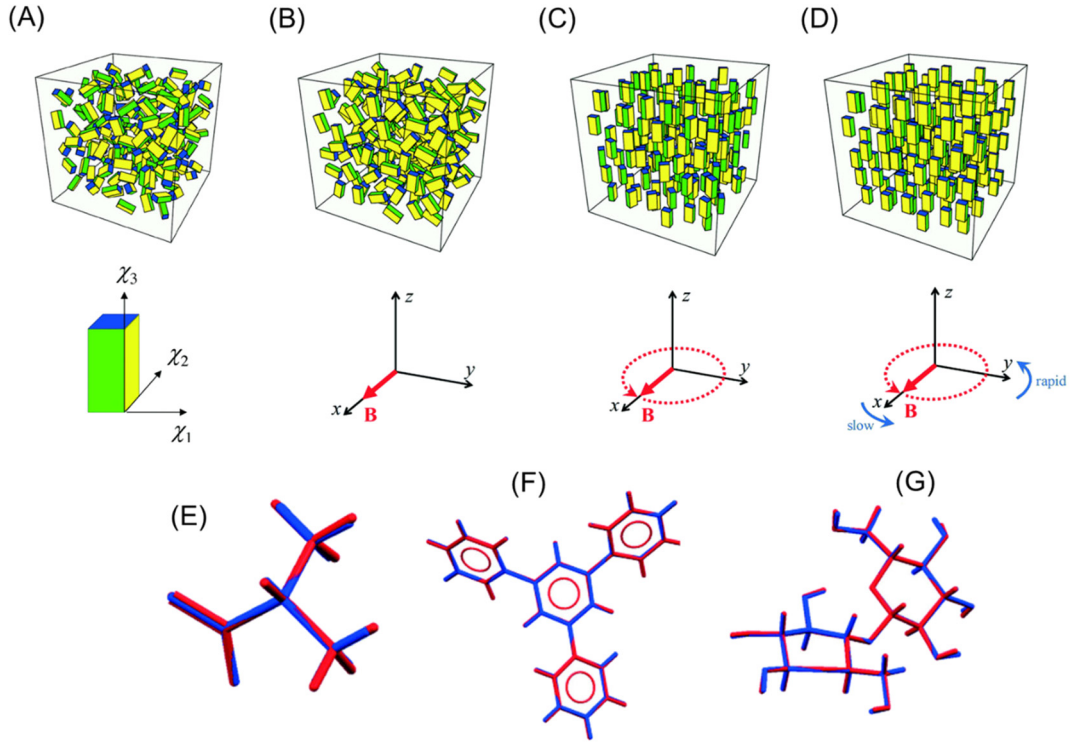

Fig. 13 Concept of the 3D-orientation by a magnetic field. The definition of three different principal values of a biaxial crystal, $\chi_1 > \chi_2 > \chi_3$, is shown in (A). (A) Random orientation under no magnetic field, (B) χ_1 axes align uniaxially in the *x*-axis under a static magnetic field, (C) χ_3 axes align uniaxially along the *z*-axis under a rotating magnetic field applied in the *xy* plane, and (D) three axes align in 3D (χ_1//*x*-axis, χ_2//*y*-axis, and χ_3//*z*-axis) under a frequency-modulated rotating magnetic field. Reproduced from ref. 197 with permission from The Royal Society of Chemistry. Comparison of the structures determined from MOMA (blue) and the structures reported previously (red): (E) L-alanine, (F) 1,3,5-triphyenilbenzene, and (G) cellobiose. Reproduced from ref. 190 with permission from The Royal Society of Chemistry.

Iwasaka *et al.*[182] demonstrated the control of the direction of the reflection by a magnetic field. This crystal can be used as a controllable mirror for analyzing microscale objects.

Liquid crystals (LCs) also have high magnetic anisotropy, and it is well known that their direction can be controlled by a low magnetic field, especially when the LCs are in the nematic phase.[183] Nematic LCs are widely utilized in displays, projectors, variable optical retarders, *etc.* The interaction between the LC and the substrate is vital to increasing the performance of these devices. The anchoring energy is a parameter to measure how the LC molecules are fixed at the interface, but the relationship between the anchoring energy and the chemical property of the substrate is not well known. Abbott *et al.* showed the behavior of LC molecules in contact with the water phase.[184,185] Depending on the solute in the aqueous phase, the preferable direction of the LC molecule at the interface changed. Yesil *et al.*[186] developed anchoring energy measurement at the LC/water interface using the magnetic orientation of LCs. The experimental setup is shown in Fig. 12A. An electromagnet (<0.5 T) was attached to a polarization microscope with a crossed-Nicol configuration. A similar optical cell to that Abbott reported was placed between the poles of the electromagnet. Then, an aqueous solution of surfactant, dodecyltrimethylammonium bromide (C_{12}TAB) or tetradecyltrimethylammonium bromide (C_{14}TAB), was added to the cell. The adsorption of the surfactant at the water/LC interface also caused homeotropic alignment. Therefore, the director of the LCs aligned to the direction of observation, and the light did not transmit to the polarization microscope (top microphotograph of Fig. 12B). Then, an external magnetic field was swept from 0 to 0.5 T. When the field strength was attained at a certain threshold, the LC alignment began. This phenomenon is the so-called Fréedericksz transition. The anchoring energy ($W_{AQ|LC}$) can be determined from the threshold magnetic field, as shown in Fig. 12C. This is the first report of the quantitative determination of $W_{AQ|LC}$, and this method will help reveal the relationship between the surface chemistry and the anchoring energy of LCs.

3.2 Alignment of diamagnetic microcrystals under a modulated rotating magnetic field

Kimura *et al.*[187] proposed a method to align diamagnetic micro-crystals three-dimensionally using a time-dependent elliptic magnetic field. They considered the magnetic alignment of a biaxial crystal, which has three different principal values, *i.e.*, $\chi_1 > \chi_2 > \chi_3$ (Fig. 13A bottom), in a viscous medium under a static and rotational magnetic field. When a static magnetic field is applied along the *x*-direction of the laboratory axis (Fig. 13B), the χ_1-axis of the crystal aligns along

the *x*-axis, whereas the χ_2 and χ_3-axes are randomly distributed in the *yz*-plane. Alternatively, where a rotational magnetic field is imposed (Fig. 13C), the χ_3-axis is oriented along the *z*-direction to minimize the magnetic potential energy, while the χ_1 and χ_2-axes are not fixed. Three-dimensional alignment can be performed by a temporally modulated rotational magnetic field (Fig. 13D), where the rotational speed is slow near the *x*-axis and fast near the *y*-axis. A detailed mathematical study of this three-dimensional orientation has been reported by Yamaguchi *et al.*,[188,189] and the optimal strength and frequency of the modulating magnetic field have been systematically discussed.

Kimura *et al.* prepared pseudo-single crystals called MOMA, which denoted a magnetically oriented microcrystal array. A suspension of microcrystals in polymer solution or UV curable resin was exposed to an elliptically rotating magnetic field. After reaching sufficient orientation, the microcrystals were immobilized by the solidification of the medium, *i.e.*, gelation or photo-curing. The MOMA sample could be handled as a single crystal. They demonstrated X-ray structure analyses of MOMAs of organic[190,191] and inorganic[192] compounds and proteins,[193–195] which were too fine to be analyzed by ordinary X-ray diffraction. Fig. 13E–G show the structure of the organic compounds determined from X-ray diffraction measurement of MOMA, which contained microcrystals of less than 50 μm. For comparison, the corresponding structures determined by using single crystals were overlapped. In each compound, the determined structures were in excellent agreement. Furthermore, they demonstrated that MOMA is applicable to solid-state NMR spectroscopy.[196]

Given that the solidification process often disarranges the microcrystals due to the anisotropic shrinkage of a gel or resin, it is preferable to measure the aligning microcrystals *in situ* in a highly viscous fluid under a modulated rotational magnetic field. Kimura and co-workers developed a technique for collecting single-crystal X-ray diffraction data from a liquid suspension, which was termed a magnetically oriented microcrystal suspension (MOMS). A magnetic orientation attachment was mounted on an in-house X-ray diffractometer to prepare the MOMS sample. Several measurement modes were proposed for the MOMS samples, such as the adjustment of the collection timing with a rotating shutter,[198] continuous rotational method,[199] and an intermittent rotation method.[200] These developments allowed the structure determination of microcrystals less than 5 μm without a synchrotron X-ray source.

3.3 Orientation of magnetic nanoparticles: observation with light

Given that MNPs have a large magnetic moment, they can be oriented in liquid by a lower magnetic field than the anisotropic diamagnetic objects. A conventional method to characterize MNPs is magnetization measurement, which is sensitive to the rotational motion of the magnetic moment due to Néel and Brownian rotations. If Néel rotation, which is the rotation of magnetic moment inside the MNP, is negligible, only Brownian rotation, which is the rotation of the particle itself, can be monitored by the magnetization measurement. It is known that a magnetic field can induce linear dichroism and birefringence in MNP samples.[201–203] The induced optical anisotropy can measure the orientation of the individual MNPs[204] along the direction of the magnetic field and the formation of chain-like aggregation.[202]

Watarai and Sakurai[205] observed that the magnetic orientational linear dichroism (MOLD) is very sensitive to the formation of small aggregates such as dimers and other oligomers of MNPs in solution. They measured the change in the MOLD spectra and shift in the maximum wavelength of COOH-modified MNP suspension by adding cationic surfactants or metal ions under a static magnetic field. The primer MNPs started to form oligomers at the critical concentration, as indicated by red arrows in Fig. 14A and B, which was defined as the "critical association concentration". The apparent association number at the cation concentration giving the maximum MOLD was evaluated for each cation from the magnetic field dependence of MOLD according to Langevin analysis. The apparent association numbers were, for example, 1.98 for Co(II) and 6.25 for Dy(III) (Fig. 14C). Then, the increase in MOLD value and the red shift in the wavelength with the addition of cation was ascribed to the formation of dimers and other oligomers, which had higher optical and magnetic anisotropy than the individual MNPs. The further addition of metal ions caused the migration and precipitation of the MNP aggregates in an optical cell. The use of the MOLD spectra of MNPs is a promising technique for detecting the association of MNPs in solution, which is valuable for the determination of the stability of colloidal systems and the design of magnetic immunoassays.

The dimerization of nanoparticles in solution is thought to be the first step in the aggregation of nanoparticles.[206] The formation of dimers is known to be highly sensitive to the zeta potential of the particle surface or immunological interactions at the surface. Prins *et al.* reported a study to use the formation of dimers of nanoparticles as two-particle nanoactuators for the rapid and sensitive detection of biomolecules.[207] Initially, biologically activated MNPs (500 nm in diameter) were incubated with the target proteins. Thereafter, a rotating magnetic field was applied to drive the formation of MNP chains. Finally, the magnetic field was removed to allow unbound nanoparticles to redisperse and the optical scattering from monomers and dimers was detected under a frequency-selective rotating magnetic field (3.5 mT, 1–5 Hz). They demonstrated a limit of detection lower than 5 pM for biotinylated BSA in human plasma in an assay time of less than 3 min. This method was applied for the analysis of prostate-specific antigen (PSA),[208] the detection of conformation switching of single native proteins,[209] and fundamental research of the kinetic mechanisms of aggregation[210] and inter-particle biomolecular reactivity.[211]

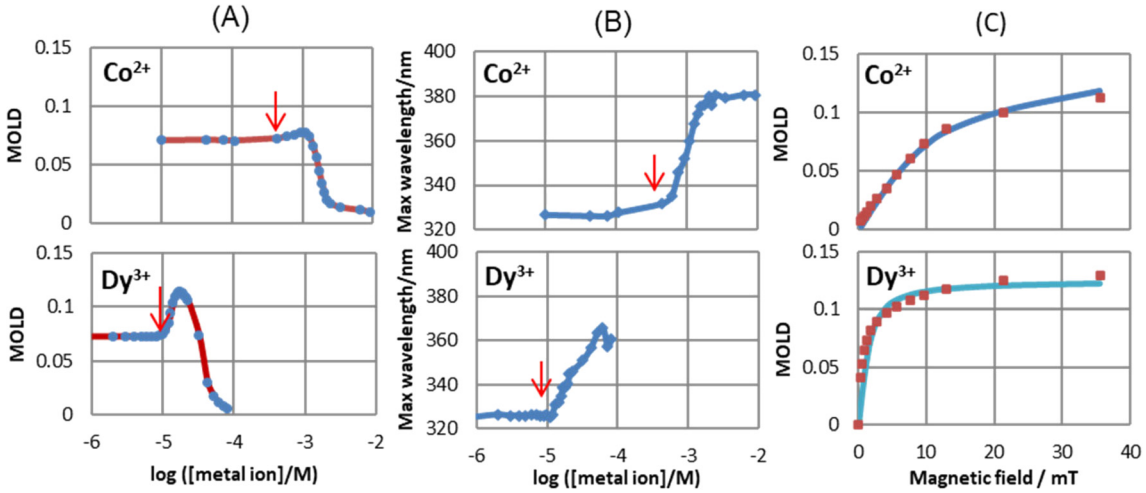

Fig. 14 Effect of metal ion concentrations of Co^{2+} and Dy^{3+} on (A) max. MOLD values and (B) max. wavelength of MOLD spectra (35.6 mT). The red arrows show the critical association concentrations. (C) Langevin analysis in $[Co^{2+}] = 9.24 \times 10^{-4}$ M and $[Dy^{3+}] = 1.67 \times 10^{-5}$ M, 0.00165 wt% MNPs. Reproduced with permission from ref. 205. Copyright © 2020, the American Chemical Society.

The response of MNPs to an alternating magnetic field ranging from kHz to MHz has been used for recent biomedical applications and nanoscale measurement techniques, such as magnetic particle imaging (MPI),[212,213] magnetic hyperthermia therapy (MHT),[214,215] magnetic particle nanorheology (MPN),[216–218] and homogeneous biosensing method.[219,220] MPI and MHT utilize Néel rotation under an ac magnetic field, whereas Brownian rotation is observed in MPN and biosensors. However, recent studies[221–227] suggest that these rotational behaviors are not independent, where the Néel rotation affects the Brownian rotation and *vice versa*. Therefore, Brownian rotation causes an unexpected signal in MPI and a change in the heat efficiency in MHT. Alternatively, Néel rotation produces a systematic error in MPN because it is assumed that the dynamic magnetization signal is completely attributed to Brownian rotation. Ota and Takemura measured the two-step magnetization response of MNPs dispersed in water by applying a fast responding pulse magnetic field, where the Brownian regime occurred after the Néel regime.[228]

Suwa *et al.* demonstrated that Brownian rotation could be measured with light under an oscillating magnetic field. They found that when a pulsed magnetic field was applied to a suspension of maghemite MNPs of 10 nm in diameter, its absorbance parallel to the magnetic field decreased.[229] For a more detailed investigation, they observed the absorbance change (ΔA) under a damped oscillating magnetic field (DOMF) in the frequency (f) range of 28.1 to 92.0 kHz.[230] Fig. 15A shows the

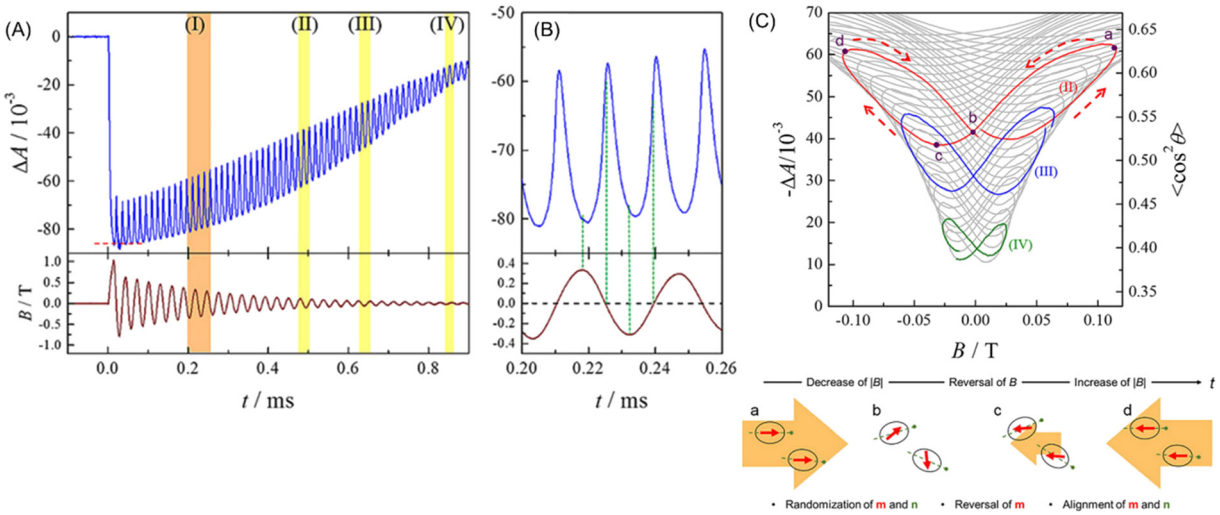

Fig. 15 (A) Typical waveform of absorbance change of MNP suspension (upper) and DOMF (bottom). (B) Enlargement of region I in (A). (C) Plots of ΔA ($\langle\cos^2\theta\rangle$) against B. The colored lines show the region highlighted in (A). Temporal direction of the curve is depicted by dashed arrows. The bottom figure illustrates the speculated behavior of magnetic moment (red arrows) and the easy axis (green dashed line) during the half period of field oscillation. Reprinted with permission from ref. 230. Copyright © 2019, American Institute of Physics.

typical waveform of ΔA, which is different from that of the DOMF (bottom panel of Fig. 15A). Specifically, ΔA has a linear relation with the degree of alignment $\langle \cos^2 \theta \rangle$, where θ is the angle between the optic axis (easy axis) and the direction of light (magnetic field) and the angle bracket indicates the ensemble average. As shown in Fig. 15C, $\langle \cos^2 \theta \rangle$ is plotted against B. This dynamic hysteresis curve directly indicates the Brownian rotation behavior of iron oxide MNPs under an oscillating magnetic field, where the MNPs keep aligning to some extent and oscillate small with $2f$. This behavior is consistent with the "magnetic mode", a predicted orientational mode for superparamagnetic nanoparticles by Usov and Liubimov[222] with a numerical simulation. Suwa *et al.* studied the size-dependence of the Brownian rotation, and they observed the "viscous mode", which is another orientational mode predicted by Usov, for the larger particles (25 nm in diameter).[231] Thus, this optical method can characterize MNPs based on the Brownian rotation in liquid. In addition, a recent study showed that this method will be useful for measuring the local viscous environment around the MNPs.[232]

4. Application of electromagnetic force

4.1 Application of electromagnetophoretic force

Kolin formulated the electromagnetophoretic (EMP) force on a particle in an electrolyte solution in 1953.[233,234] When a homogeneous electric current is applied through a closed conductive solution containing a particle under a homogeneous magnetic field perpendicularly applied to the electric current, the force is exerted on both the medium and the particle. Here, two forces act on the particle. The Lorentz force directly working on a particle is called the electromagnetic weight (EMW), F_{EMW}. The Lorentz force on the medium that works on the particle as an equal magnitude and opposite directional force is called the electromagnetic buoyancy (EMB), F_{EMB}. The electromagnetophoretic force, F_{EMP}, exerted on a particle having a volume, V (m^3), in a closed cell with an inner sectional area of S (m^2) is expressed as the sum of F_{EMW} and F_{EMB}, as follows:

$$F_{\mathrm{EMP}} = F_{\mathrm{EMW}} + F_{\mathrm{EMB}} = \frac{3}{2} BV \left(\frac{\sigma_{\mathrm{p}} - \sigma_{\mathrm{f}}}{2\sigma_{\mathrm{f}} + \sigma_{\mathrm{p}}} \right) \frac{i}{S}, \qquad (12)$$

where B is the magnetic flux density ($\mathrm{N\ A^{-1}\ m^{-1}}$), σ_{p} is the electric conductivity ($\mathrm{S\ m^{-1}}$) of the particle, σ_{f} is the electric conductivity ($\mathrm{S\ m^{-1}}$) of the medium, and i is the current (A).

4.1.1 Electromagnetophoresis of particles. Pioneering work in the application of electromagnetophoresis for the fractionation of biological cells has been reported by Kolin and Kado.[234] Three biological particles of red blood cells (*ca.* 4 μm in radius), lycopodium spores (*ca.* 15 μm in radius), and sea urchin eggs (*ca.* 60 μm in radius) were fractionated depending on the size and the conductivity as sharp zones with 3 mm each separation distance after 2 min performance. The magnetic field of 600 mT and the current density of 100 mA $\mathrm{cm^{-2}}$ were applied in phase by an alternating current of 60 Hz. The use of alternating currents can induce unidirectional migration and simplify the design of the migration cell. The expected thermal and electromagnetic convection were effectively inhibited by establishing a steep density gradient with sodium chloride in the migration column. However, the temperature of the medium increased by 5 °C after the 2 min fractionation performance. Ozawa *et al.* studied the effect of magnetic field on the electrophoresis of DNA and suggested the role of Lorentz force.[235] As pointed out by Kolin, heat dissipation is needed to stabilize the migration performance of electromagnetophoresis. Namba and Watarai used a silica capillary as an effective way to reduce the Joule heating. In a micro-capillary system, the EMP buoyancy was enough to migrate polystyrene particles (3 μm, 15 μm, and 22 μm in diameters) in 0.105 T.[236] The migration velocity, v, depended on the second power of the microparticle radius, r, and was linearly dependent on the electric current and magnetic flux density, as expected from the equation, as follows:

$$v = \frac{4}{9} \left(\frac{\sigma_{\mathrm{p}} - \sigma_{\mathrm{f}}}{2\sigma_{\mathrm{f}} + \sigma_{\mathrm{p}}} \right) \frac{iBr^2}{S\eta}, \qquad (13)$$

where η is the fluid viscosity (Pa s). The apparent conductivities of polystyrene particles were estimated using the above-mentioned equation to be 0.030–0.045 $\mathrm{S\ cm^{-1}}$ in 1.0 M KCl solution, which was thought to correspond to the surface conductivity of the particles. When the magnetic field was not homogeneous, radial circulation of the medium occurred in the capillary due to the magnetic hydrodynamic (MHD) flow.[197]

Iiguni and Ohtani determined the surface conductivity of an organic droplet in an aqueous solution of cetyltrimethylammonium bromide (CTAB) from the measurement of the electromagnetophoretic velocity of the droplet under a magnetic field of 1 T and electric current of 40–110 μA. An increase in CTAB concentration resulted in an increase in the surface conductivity.[237] It will be interesting to investigate the relationship between the surface conductivity observed by electromagnetophoretic velocimetry and zeta potential of the droplet.

Chromatographic application of EMP force to a particle separation was investigated by Iiguni and Watarai, which was called electromagnetophoretic adsorption–desorption chromatography in a capillary flow system.[238] The principle is the combination of the Stokes viscous force generated by the liquid flow and the adsorption–desorption migration across the inside of the capillary caused by the electromagnetophoretic buoyancy induced by the applications of an alternative current and a homogenous magnetic field (Fig. 16A). When the electric current direction was switched periodically, the test polystyrene particles showed "zigzag" migration behavior, mainly depending on the particle size and desorption force from the capillary wall. Employing this method, the polystyrene particles of 10 μm and 20 μm in diameter dispersed in 1 M KCl solution containing 0.01% Triton X-100 were separated using only a 1

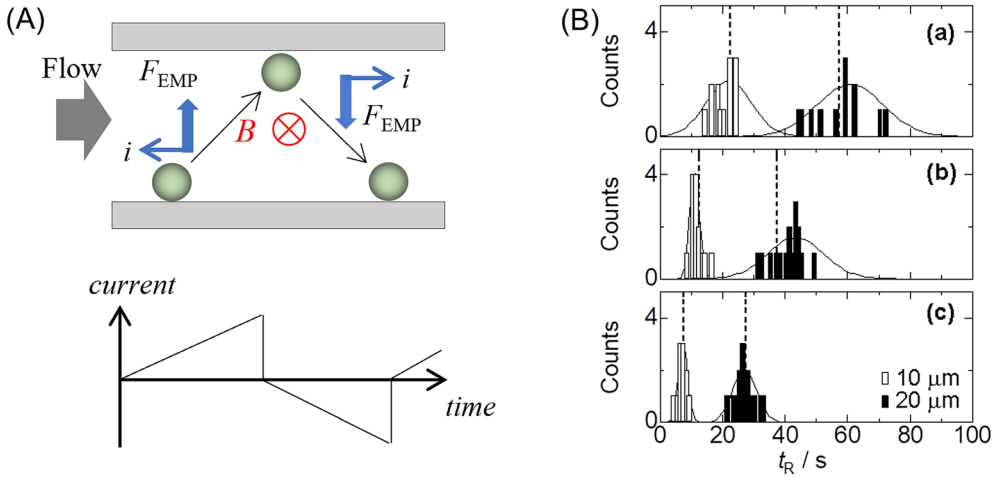

Fig. 16 (A) Schematic drawing of the concept of adsorption–desorption EMP chromatography working under a switched electric current, *i*. (B) Chromatograms of polystyrene particles under the flow rates of (a) 60, (b) 80, and (c) 100 μL h^{-1} with 2000 max μA (0.5 Hz) and 10 T. Reproduced with permission from ref. 238. Copyright © 2005 m Elsevier B.V.

mm long fused-silica capillary with the inner diameter of 200 μm under a homogeneous magnetic field of 10 T. The best resolution of 1.90 was attained under the conditions of maximum current of 2000 μA switched with 0.5 Hz and flow rate of 100 μL h^{-1} (Fig. 16B).

Iiguni *et al.* studied electromagnetophoresis in microchip systems using hydrodynamic focusing in the sample inlet part to separate different-sized polystyrene particles (3, 6, and 10 μm in diameters) and between yeast cells and polystyrene particles. However, the hydrodynamic focusing required a large amount of sheath solution.[239] To overcome this disadvantage and improve the separation efficiency, they fabricated a microchip system composed of a 7 mm EMP focusing segment and 3 mm EMP separation segment, where the two EMP forces were applied inversely.[240] To keep the sample particles in a single flow channel, a micro-dialysis hollow fiber (o.d. 220 μm, i.d. 200 μm, molecular cut-off: 13 kDa) was used in the microchip. An injected mixture of particles was focused to one side in the focusing segment of the hollow fiber channel, and then the particles were migrated in opposite direction, with the velocity depending on the size, and finally fractionated by the Y-shaped outlet channels. Consequently, 87% of 3 μm polystyrene particles was isolated from a mixture of 3 and 10 μm particles.[201]

A magnetic field and an electric current were postulated to be uniform in a simple analysis of the EMP velocity, but the uniformity of the electric current density changed when the micro-flow system included non-conductive microparticles or emulsions in a conductive medium. The ionic current density profile inside the channel was greatly changed by the presence of this droplet, and the EMP force around the droplet became complicated. Funaki *et al.* observed a curious micro-convection of smaller organic droplets around a larger organic droplet in a capillary electromagnetophoretic system.[241] When the electric current of 0.5 or 1.0 mA was applied at 3.5 T or 2.7 T, larger droplets became arranged at regular intervals on the capillary wall, and smaller droplets circulated around the larger droplets (Fig. 17). This behavior was explained by the difference in the local electric current density around a larger droplet, which was lowest on both electrode sides of the droplet, leading to the circulation of

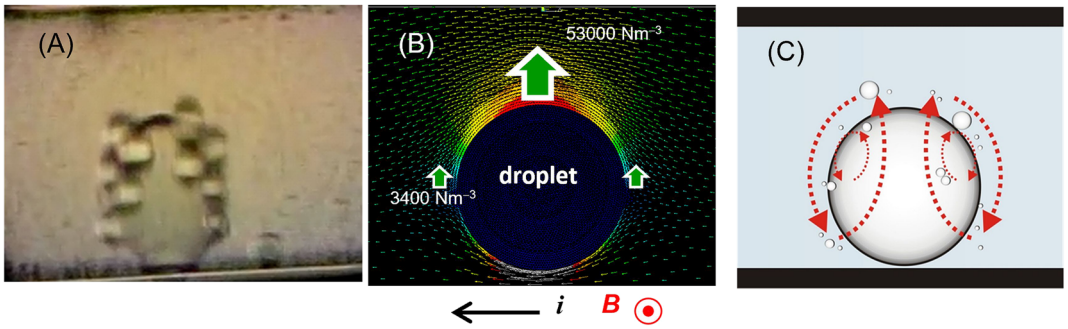

Fig. 17 Behavior of organic droplets in a capillary (100 μm i.d.) in a superconducting bulk magnet system (3.5 T) observed from the direction parallel to the magnetic field. (A) Rotation of smaller droplets around a larger droplet at 500 μA. (B) Simulation of Lorentz forces exerted to the top and side regions of a 10 μm droplet at 1 mA. (C) Schematic illustration of the orbitals of smaller droplets due to local electromagnetophoretic convection. Dodecane was 20% in volume with 0.2 mM Triton X-100 in 1 M KCl solution. Reprinted from ref. 241.

the medium due to the inhomogeneity of the Lorentz-force around the larger droplet.

4.1.2 Electromagnetophoretic dynamic force measurement. Dynamic force measurement methods, such as hydrodynamic-flow-based method, laser tweezers, and atomic force microscopy (AFM), have been used to investigate the molecular interaction between two different cell surfaces. However, these methods still have some problems in the fine control of the applied force and require complicated sample pretreatment. As an alternative method, electromagnetophoretic (EMP) force measurement was reported by Iiguni and Watarai.[242,243] Detachment events of single polystyrene particles from the inner wall of a capillary in an electrolyte solution can be observed with an optical microscope by controlling the electromagnetophoretic buoyancy working on the particles. These single-event measurements must be repeated enough times to get the relevant distribution result from a histogram. This technique has been applied to the dynamic force measurements of a single binding interaction between lectin and mannan polysaccharide on yeast cell surfaces.[244]

Kato *et al.* developed electromagnetophoretic dynamic force measurement for the detachment dynamics of microparticles adsorbed on the inner wall of a silica capillary. Especially, the COOH-modified polystyrene particle–wall interaction in electrolyte solutions was studied by changing the pH and the concentration of coexisting metal ions of Cu^{2+}, Ni^{2+}, Fe^{3+}, or Al^{3+} on the desorption dynamics under a 10 T magnetic field.[245] They derived the equation for the dynamic force analysis based on the model of Bell,[246] as follows:

$$\frac{1}{t}\ln\frac{N(0)}{N(t)} = k_{\mathrm{off}}(0)\left(1+\frac{A}{2}t+\frac{A^2}{6}t^2+\ldots\right), \qquad (14)$$

where t is the loading time of external force, $N(0)$ and $N(t)$ are the number of the total bound particles to the wall and the number of the undetached particles after time t, $k_{\mathrm{off}}(0)$ is the rate constant for the dissociation of the interaction in the absence of the pulling force, and $A = r_F\Delta x/k_BTN_b$, where r_F is the increasing rate of the pulling force (pN s^{-1}), Δx is the increment of the bond length from the equilibrium state to the critical transition state under the pulling force, k_B is the Boltzmann constant, T is the absolute temperature, and N_b is the number of chemical bonds between a single particle and the wall. Fig. 18A shows a typical histogram of the desorption events of 10 μm carboxyl-modified polystyrene particles. The analysis of the histogram using the above-mentioned equation gave the values of $\Delta x/N_b$ and $k_{\mathrm{off}}(0)$ as 0.03 nm and 0.10 s^{-1}, respectively. This method can be adapted to a microchip system as a simple dynamic force measurement technique of chemical interactions given that it works in a closed micro-solution system with high measurement repeatability and precise non-contacting control of the pulling force.

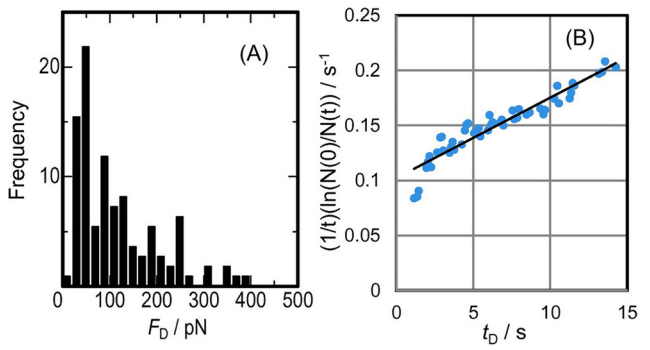

Fig. 18 (A) Histogram of the desorption events of 10 μm COOH-modified polystyrene particles by electromagnetophoretic pulling force at a rate of 16.1 pN s^{-1} at pH 7.1. (B) Dynamic force analysis of the detaching event shown in (A) by eqn (14), giving the values of $\Delta x/N_b$ = 0.03 nm and $k_{\mathrm{off}}(0)$ = 0.10 s^{-1}. Reprinted with permission from ref. 245. Copyright © 2016, The Chemical Society of Japan.

The effect of an external force on the structural equilibrium of a biological molecule was investigated by Wakiyama and Watarai.[247] The pulling force due to the electromagnetophoretic buoyancy was applied to stretch cysteamine molecules bound between a polystyrene particle and Ag nanoparticles on a glass substrate. The SERS spectra of cysteamine observed under the pulling force of 81 pN showed an increase in the *trans*/*gauche* ratio, suggesting a shift in the conformational equilibrium to the *trans* form side by the pulling force, as observed in the magnetophoretic dynamic force measurement.[90]

4.2 Electrochemical systems

4.2.1 Magnetohydrodynamic (MHD) flow. Electroanalytical chemistry has been widely developed because of its excellent flexibility and adaptability in analytical instrumentations for detecting redox reactions under precise control of the voltage and/or current of the working electrode. Also, its broad applicability to biological and industrial samples is a great advantage. However, the application of a magnetic field to electrochemical systems has only emerged recently, as reviewed by Monzon and Coey.[248] Aogaki *et al.* reported in 1975 that magnetohydrodynamic (MHD) flow was observed inside a copper electrode immersed in an electrolyte solution (0.5 M $CuSO_4$–0.5 M H_2SO_4) due to the Lorentz force streaming of the medium when a magnetic field was applied parallel to the electrodes, as schematically shown in Fig. 19A.[249,250] Later, they discussed the different roles of two types of nonequilibrium fluctuations for micro-magnetohydrodynamic (MHD) effects observed in a surface reaction of copper deposition under a magnetic field parallel to the electrode surface.[250] Asymmetrical concentration fluctuation, which occurs in an electric double layer, controlled the 2D nucleation with a diameter in the order of 10–100 μm. Symmetrical concentration fluctuation, which occurs in a diffusion layer, controlled the 3D nucleation on 2D nuclei in the order of 0.1 μm. They theoretically discussed the new types of micro-magnetohydrodynamic (MHD) effects arising from the unstable growth of three-dimensional (3D) and two-dimensional (2D) nuclei by specific adsorption of hydrogen ions (second micro-MHD effect).[251,252]

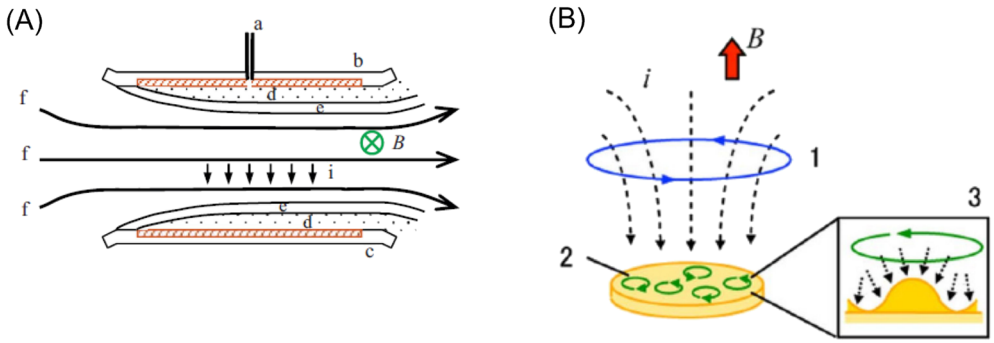

Fig. 19 (A) Schematic configuration of the MHD electrode where the magnetic field is applied parallel to the electrode. a: Luggin capillary, b: working electrode, c: counter electrode, d: diffusion layer, e: hydrodynamic boundary layer, and f: streaming. Reprinted with permission from ref. 250. Copyright © 2009 Elsevier B.V. (B) MHD electrode where the magnetic field was applied vertically to the electrode. 1: vertical MHD flow around the electrode edge, 2: micro-MHD vortices and 3: schematic of the micro-MHD vortex around the non-equilibrium fluctuations (humps) on the deposit surface.[254] Reprinted with permission from ref. 259. Copyright © 2014, The Polish Physical Society.

The MHD effect was also studied on electrodeposition in a vertical magnetic field configuration, where a magnetic field, B, and current, i, were applied perpendicularly to the electrode surface.[253,254] Two types of MHD flows were proposed by Aogaki's group, as shown in Fig. 19B. One is the macroscopic MHD flow around the electrode edge, where the ionic currents are not parallel to the magnetic fields. This is termed vertical MHD flow (Fig. 19B1). The other is the micro-MHD vortex around the local bumps and micro-dents formed by nonequilibrium fluctuation in electrodeposition (Fig. 19B2). Then, the surface morphologies of the magneto-electrodeposition films exhibited micro-circular structures, suggesting the existence of micro-MHD vortices.[248,254,255] Recently, the dominant role of the global (vertical) MHD flow compared to the micro-local MHD flow has been shown in the formation of nm-sized cones in the electrodeposition of nickel layers on a copper working electrode.[256] In addition to the importance of Lorentz force in electrochemical systems, the role of Kelvin force has been clarified in the electrodeposition of micro-structured copper layers.[257,258]

4.2.2 MHD pumping. The most common flowing principle in microfluidic systems is electrokinetic (electroosmotic) pumping. However, electrokinetic flow requires a high voltage of about 100 V, which may cause bubble formation due to water electrolysis and is highly dependent on the zeta potential of the wall surface. As an alternative principle, MHD convection on the surface of the electrode was demonstrated by using an Nd–Fe–B magnet, where a magnetic field was applied parallel to the disk electrode surface. The effect of MHD convection showed a similar improvement to the rotating disc electrode.[260] MHD actuation using a 1 kHz ac signal was investigated to avoid issues of net reactant migration, leading to electrode and reactant degradation, and the accompanying generation of electrolytic bubble. Thus, a fluid velocity of 300 μm s^{-1} in 500 mM KCl solution was attained.[261] The advantages of MHD pumping in microfluidic systems were reviewed by Qian and Bau.[262]

4.2.3 Electrochemistry with MHD. Fritsch's group made a remarkable contribution to the application of the MHD effect in electroanalytical chemistry. In 2004, Clark and Fritsch reported the novel application of redox-MHD, which enhanced the current in anodic stripping voltammetry of some metal ions.[263] Redox MHD effectively enhanced the linear scan anodic stripping voltammetry signals by inducing convection during the preconcentration step. They demonstrated dc redox MHD pumping in microchannels (270 μm wide × 640 μm deep × 2 cm long). Flow velocities of up to 5.0 mm s^{-1} were observed in a solution of 0.5 M nitrobenzene and 0.5 M tetrabutylammonium hexafluorophosphate ($TBAPF_6$) in acetonitrile using a 0.41 T Nd–Fe–B permanent magnet, at an applied voltage of −1.3 V *vs.* Ag/AgCl.[264] The corresponding current enhancement was as large as 145%. As the reversible redox pairs, two solutions of 0.125 M Fe^{2+} and 0.125 M Fe^{3+} in 3.0 M KCl and 0.125 M $FeCN_6^{3-}$ and 0.125 M $FeCN_6^{4-}$ in 2.0 M KCl were investigated.[264,265]

The earlier applications of MHD force in analytical chemistry were reviewed by Fritsch *et al.* in 2010.[266]

Recently, this group successfully eliminated the need to add redox species to the solution for the MHD pumping by the use of the electrode modified with a conductive polymer, thus removing interferences with detection, sample, and reagents for lab-on-a-chip applications.[267,268] A conductive polymer, poly(3,4-ethylenedioxythiophene) (PEDOT), was electropolymerized on microband gold electrodes in a solution consisting of 0.010 M EDOT, 0.010 M SDS, and 0.100 M KCl (ref. 267) or in solutions containing 0.010 M EDOT and 0.100 M $TBAPF_6$ or $LiClO_4$ electrolyte, respectively, in propylene carbonate.[268] At the anode, PEDOT was changed from the neutral to oxidized state, which was associated with ions moving into or out of the film from the surrounding solution to compensate for the change in charge. At the cathode, PEDOT was converted from its oxidized state to its neutral state, causing the anions to leave the PEDOT film and enter the surrounding solution. This redox reaction generated an ionic current in the solution, leading to the MHD flow of the solution, as shown in Fig. 20A. When a 0.37 T magnet was used, fluid speeds of 590 μm s^{-1} were observed

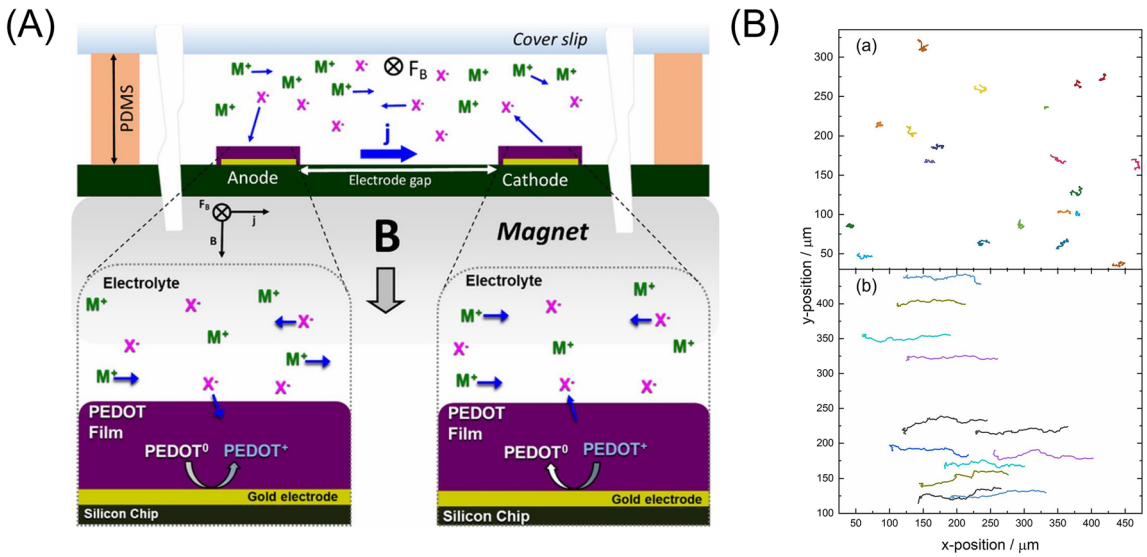

Fig. 20 (A) Illustration of the generation of MHD fluid flow by PEDOT-modified electrodes, which produced an ionic current, *j*, between anode and cathode upon application of an electronic current, and in a chamber containing electrolyte of M^+ and X^- ions over a permanent magnet, providing *B*. M^+ and X^- refer to cations and anions, respectively. Reprinted from ref. 268. (B) Effect of 1-D MHD flowing in the tracking of the mixed NP suspension in 50 mM KNO_3 over 74 frames (7.4 s) during an applied current of +50 μA and in the (a) absence and (b) presence of a magnet (flow direction to positive *x*-positions). Reprinted from ref. 270.

immediately after applying a potential step.[267] The conductive polymer redox MHD pumping was combined with an epitaxial light sheet confocal microscope to observe three types of leukocyte samples.[269] Recently, their redox magnetohydrodynamics (RMHD) microfluidics was coupled with dark-field microscopy to offer high-throughput single-nanoparticle (NP) differentiation in a flowing mixture of 82 nm Ag and 140 nm Au-coated silica particles by localized surface plasmon resonance and tracking of NPs (Fig. 20B). The well-controlled RMHD pumping enabled a continuous, reversible, and uniform flow for precise and simultaneous NP tracking of the Brownian motion.[270]

4.2.4 Effects of MHD and spin-selectivity on water splitting. Water splitting or water electrolysis is a well-known electrochemical reaction to produce molecular hydrogen and molecular oxygen from water. The application of a uniform external magnetic field to the electrodes can enhance bubble production and the role of the magnetic field was explained by the MHD effect, which induces localized magnetic stirring and accelerates the flow between the electrodes.[271] However, currently, the understanding of the physicochemical mechanism of the gas nucleation from solution is still very limited.[248]

Naaman *et al.* synthesized chiral Fe_3O_4 NPs by adsorbing chiral molecules on the surface of NPs to induce chiral catalytic activity and used them as a spin selective anode in photoelectrochemical water splitting with visible light.[272] The water splitting could be performed with an electric current as high as 10 mA cm^{-2}, and the H_2O_2 evolution was reduced. The role of chiral molecules, which were D- and L-tryptophan and L-alanine peptides, was explained as the spin filter. Recently, the effect of a magnetic field on the oxygen evolution reaction was quantitatively studied using a cobalt oxide|fluorine-doped tin oxide-coated glass anode, and a 4.7% increase in the anodic current at 1.5 V was observed at the magnetic field of 371 mT.[273] The magnetic field effect was separated into two distinct regions, depending on if the magnetic flux density was lower or higher than 40 mT, but the physical origin of the two regions was not clear. Suda *et al.* prepared a spin-selective and high-conductive chiral MoS_2 electrode by intercalating (*R*)-(+)-α-methylbenzylamine or (*S*)-(−)-α-methylbenzylamine. The chiral molecule-intercalated multilayers could achieve spin polarization as high as 75%. The spin selectivity suppressed the production of H_2O_2 and promoted the formation of ground-state O_2 molecules.[274] Hydrogen production from water splitting is a recent hot subject related to the global Carbon Neutral Project.

4.3 Chiral selectivity in magneto-electrochemistry

The electromagnetic force or Lorentz force induces rotational motion, as observed in the cyclotron motion of charged particles in a magnetic field. On the surface of the working electrode, electromagnetic force generates hydrodynamic helical motion of electrolyte solution depending on the direction of the magnetic field and the current, which are both applied vertically to the electrode (Fig. 19B of 4.2). Mogi *et al.* discovered that a polyaniline film prepared on a Pt working electrode by magneto-electropolymerization (MEP) under the conditions of a magnetic field of 5 T and a passing charge of 0.1 C cm^{-2} exhibited enantioselectivity when the polyaniline film electrode was used in the cyclic voltammetry measurement of L- and D-ascorbic acids (AA).[275] The current

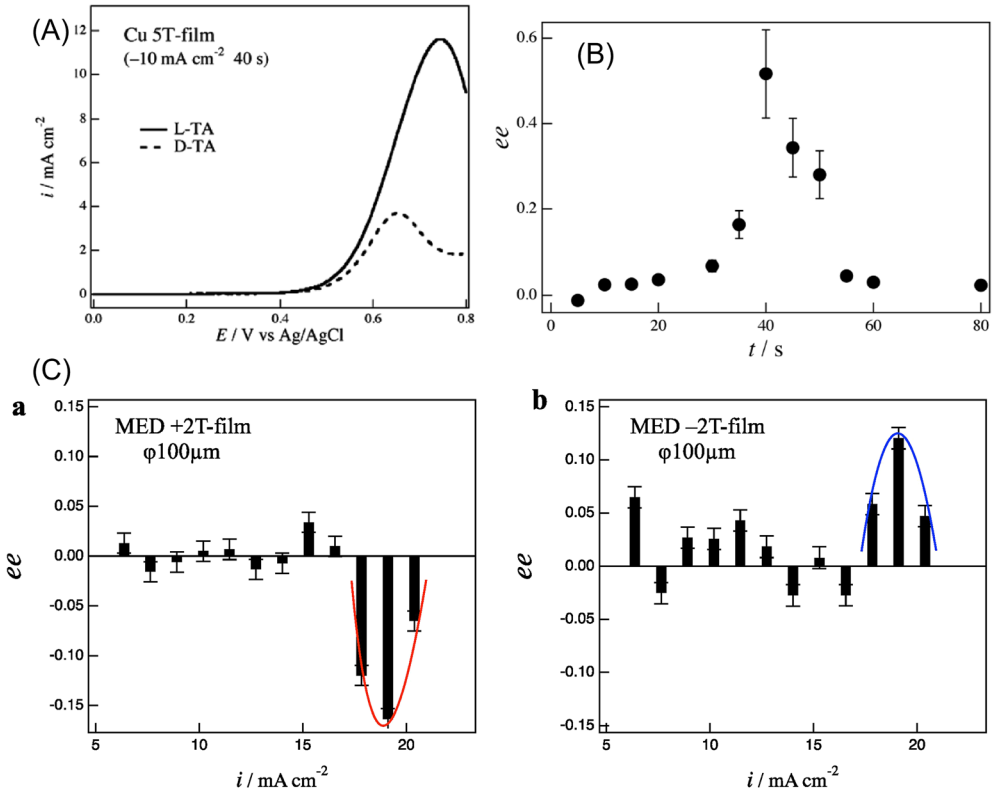

Fig. 21 (A) Voltammograms of 20 mM L- and D-tartaric acid (TA) under 50 mV s^{-1} in Cu 5 T-film electrode in 0.1 M NaOH with 40 s deposition time.[259] (B) Enantioexcess (ee) *vs.* magneto-electrodeposition time. Reprinted with permission from ref. 259. Copyright © 2014, The Polish Physical Society. (C) ee ratio *vs.* deposition current on a 100 μm electrode: (a) +2 T film and (b) –2 T film. Reprinted from ref. 277.

of the oxidation peak of L-AA at 0.4 V was larger than that for D-AA on the film electrode prepared at +5 T. The result was the opposite on the −5 T-film electrode, where the peak current for D-AA was larger than that for L-AA. The ability of enantioselective recognition of the polyaniline film depended on the direction of the magnetic field. They thought that the Lorentz force may act on the currents in the polymer chains and induce helically coiled structures of the polymer chains. They also observed that the Cu film produced by magneto-electrodeposition under 5 T showed chiral selectivity in the cyclic voltammetry of tartaric acid (TA) (Fig. 21A).[259] The enantiomeric excess (ee) ratio in the voltammograms, which is defined as ee = $(i_p^L - i_p^D)/(i_p^L + i_p^D)$, where i_p^L and i_p^D represent the peak currents of L- and D-TA, respectively, gave positive values during 30–50 s deposition time (with a maximum value of 0.5 at 40 s), where the steady self-organized state of the MHD flows formed on the surface of the Cu film electrode. These facts implied that the self-organized state of the micro-MHD and the vertical MHD flows are crucial for the formation of chiral Cu film surfaces (Fig. 21B).[259] Furthermore, they found that the specific adsorption of chloride ions on the film surfaces and the direction of the magnetic field of 5 T had a drastic influence on the chiral property of the Cu film, which was measured by the voltammetric ee ratio of L- and D-alanine. They suggested that not only the micro-MHD vortices but also the rate-limiting steps of Cu dislocation are responsible for the chiral surface formation.[276] Recently, they investigated the effect of the working electrode diameters of 25, 100, and 3000 μm on the chiral selectivity of a Cu film prepared under the magnetic fields of 1–5 T. The results suggested that the strong vertical MHD flows can induce the breaking of the chiral structure of the Cu film through the fluctuation of the micro-MHD vortices.[277] Further studies are anticipated on the fabrication of other chiral electrodes and the relationship between the nanostructure of the electrode and the chiral selectivity in the electrode reaction.

Besides the micro-MHD vortex mechanism for chiral electrodeposition, Naaman's group reported another principle to generate enantio-selective interaction between chiral molecules and a perpendicularly magnetized ferromagnetic electrode, which is known as the chirality-induced spin selectivity (CISS) effect.[278,279] When electrons move through chiral molecules, their transport velocity is spin-dependent given that the preferred spin orientation is determined by the handedness of the molecule and the direction of motion.[279] They demonstrated the enantioselective adsorption of L- or D-polyalanine (PAL)-based oligomer (thiolated α-helix oligopeptide) when its solution was exposed for 2 s in 0.3 T to a ferromagnetic (FM) cobalt film covered with 5 nm of gold.[280] In one magnetization direction, the L-PAL adsorption rate was 8-times faster than that of D-PAL. In contrast, in the other magnetization direction, the D-PAL adsorption rate was 4 times faster than that of L-PAL (Fig. 22A). However, the D-PAL purification level was lower than that of L-PAL, indicating the asymmetry in

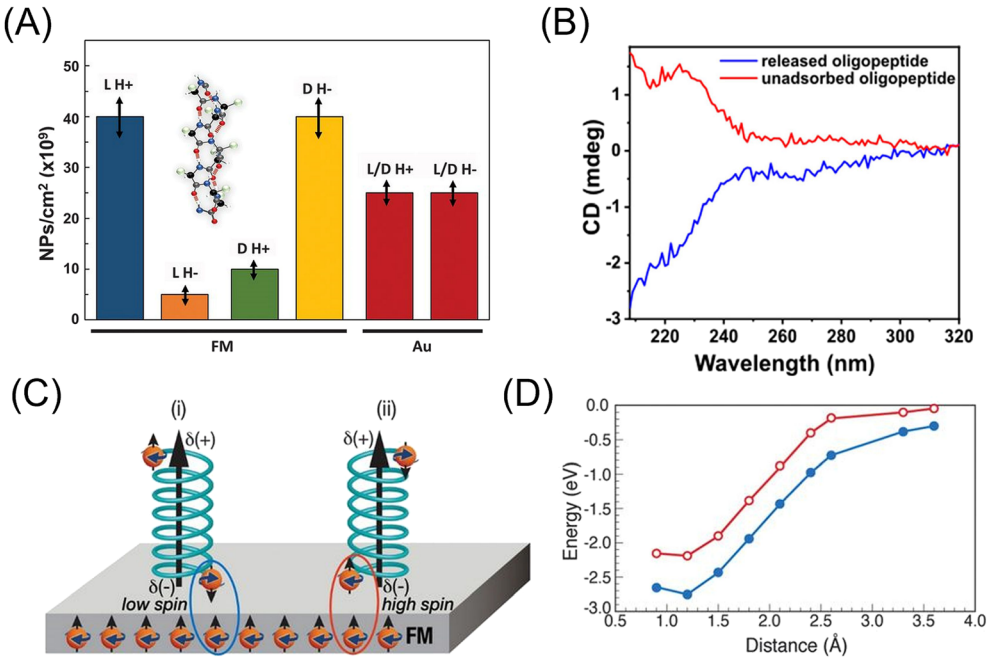

Fig. 22 (A) Enantio-specific adsorption from L- and D-oligopeptide solutions after exposure for 2 s shown by the SiO_2 nanoparticle adsorption density, which was compared with the adsorption density on Au with an applied external magnetic field of up (H+) or down (H–). Reprinted with permission from ref. 280. Copyright © 2018, The American Association for the Advancement of Science. (B) CD spectra of the racemic oligopeptide after passing through the separation system (red line) and the electrochemically desorbed oligopeptide from the ferromagnetic surfaces (blue line). Reprinted from ref. 282. (C) Electrical polarization of the molecule is accompanied by spin polarization. The spin alignment at each electric pole depends on the specific enantiomer. Therefore, the interaction between the magnetized Ni surface and the molecule (circled in blue and red) follows either a low-spin (i) or a high-spin (ii) potential, depending on the direction of magnetization of the substrate. Reprinted with permission from ref. 280. Copyright © 2018, The American Association for the Advancement of Science. (D) Interaction energies between Ni substrate and H atom calculated by DFT as a function of the distance between a hydrogen atom and a surface. In the calculation, all spins of the Ni atoms are aligned parallel to each other, and the H atom spin is aligned either parallel (red curve) or antiparallel (blue curve) to the spin of the Ni atoms. Reprinted with permission from ref. 280. Copyright © 2018, The American Association for the Advancement of Science.

adsorption rate ratios. A longer adsorption time of 2 min resulted in a reduction in the enantio-selectivity of adsorption, suggesting that the process includes substantial kinetic differences. When a racemic PAL mixture was exposed to a magnetized substrate (1 cm × 1 cm), upon sequential exposure to 100 substrates with up- or down-pointing magnetization (0.3 T), a clear CD spectrum corresponding to D- or L-PAL, respectively, was obtained from the residual solution. The results indicated that the L-enantiomer favors the surface that is magnetized up, whereas the D-enantiomer favors the down magnetization. The spin-selective interaction between the enantiomer and the substrate was explained using DFT calculation (Fig. 22C and D). Naaman's group extended their study to the enantio-selective separation of small molecules. An ultrathin Ni (5 nm)/Au (10 nm) film coated with an achiral self-assembled monolayer (SAM) of carboxyl-terminated alkanethiols [$HS–(CH_2)_{x-1}–COO^-$] was exposed to 1 mM solution of both (*R*)- or (*S*)-1-amino-2-propanol for different interaction times under magnetized either parallel (up) or antiparallel (down) with respect to the substrates. The OH-stretching band of the 1-amino-2-propanol-SAM adduct formed on the surface of Ni film was monitored by infrared (IR) spectroscopy as a function of the substrate magnetization (either up or down by 0.5 T magnet), and the incubation time. Maximum adsorption of (*S*)-1-amino-2-propanol was observed after 2 min for the down magnetization, but that of (*R*)-1-amino-2-propanol adsorbed more strongly after 10 min for the up magnetization. This selectivity was effective for 30–40 min, and no discernible difference was found for longer adsorption times. According to the study by changing the number of CH_2 groups, it was found that the spin-exchange interaction decays at a distance of 0.75 nm from the ferromagnet-gold-covered surface. A gold (10 nm)-coated Ni (120 nm) electrode with a 1.0 nm SAM of 1-hexanethiol was used as the working electrode for the electrochemical oxidation and reduction of (*R*)- and (*S*)-ferrocene in solution, injecting electrons with their spin-polarized parallel (down magnetization) or antiparallel (up magnetization). The cyclic voltammogram showed a clear dependence of the direction of the magnetization, suggesting the enantio-selectivity associated with the helicity of the electron. The effect of spin injection was also observed in the electrochemical reduction of camphor sulfonic acid.[281] Based on the two principles of (1) chiral-induced spin selectivity, which allowed the selective adsorption of one enantiomer on a perpendicularly magnetized substrate, and (2) the release of the adsorbates electrochemically, the enantioselective separation method of a racemic mixture of thiolated molecules was developed by applying ferromagnetic surfaces (Fig. 22B).[282]

Both phenomena, the micro-MHD vortex-induced chiral selectivity reported by Mogi *et al.* and the spin-induced chiral selectivity reported by Naaman's group, have provided exciting subjects in the field of magneto-electrochemistry and chiral materials science. Future research on the *in situ* measurement of the surface chiral reactions will clarify the mechanism of the spin-selective effect in the enantio-selectivity of an electrodeposited film fabricated under micro-MHD conditions. Besides, enantio-selective separation using an electromagnetic field or spin selective interaction will be valuable for constructing novel micro-flow analytical systems.

5. Conclusion and perspective

In the last two decades, magnetophoretic force, magnetic orientation force, and electromagnetophoretic force have been applied to various analytical systems. However, the utility of these forces is not well understood in the field of analytical chemistry, and thus it should be further investigated in future studies. The unique feature of magnetic gradient force and magnetic orientation force is that these forces depend on the magnetic susceptibility of the analytical samples, which can be used for the determination of their components. However, to date, the development of this feature is in its infancy. Another important feature is that any of three forces can work more effectively on a microparticle than on molecules or ions in solution because the forces are proportional to the volume of the samples. Therefore, biological particles such as cells and DNA can be directly migrated or manipulated by these forces. For the separation and detection of molecules and ions, nano/micrometer-sized particles or composites need to be used as chemical mediators. In this regard, functional MNPs have been designed and synthesized as highly sensitive analytical probes for biosensing.[22]

A high magnetic field and/or high magnetic field gradient are generally preferred to attain high performance in magneto-analytical methods. Electromagnets (<1 T) or superconducting magnets (5–15 T) are suitable to serve a homogeneous magnetic field, but small permanent magnets (<0.5 T) are commonly used for micro-analytical and electrochemical systems because of their excellent usability in small instruments. However, it should be noted that the magnetic field generated by a permanent magnet is inherently inhomogeneous. Therefore, not only the Lorentz force but also the magnetic gradient force should be carefully considered in electrochemical systems. In addition, the magnetic field dependence of the analytical performance is not always investigated, especially in studies using permanent magnets. The measurement of magnetic field dependency should be recommended to understand the mechanism of magnetic field effect and to determine the optimum magnetic field. A magnetic circuit composed of permanent magnets, which can generate a high magnetic field of more than 3 T (ref. 51) and a one-dimensional uniform magnetic field[283] should be used more widely, combined with microscopic observations. Permanent magnets also provide a high magnetic field gradient to levitate a micro-water droplet.[65,284] Furthermore, a rotating magnetic field by quadratic electromagnets[15] and a frequency-modulated rotating magnetic field[192] were used to rotate and orient submicron- and micro-particles. Electromagnets are especially suitable for providing an ac magnetic field. A pulsed magnetic field higher than 10 T and shorter than 1 ms can be generated by a rather simple electromagnet with a power supply. A pulsed magnet is recommended for observing magneto-optical effects such as Faraday rotation of solution samples[285–287] and can be used to measure the magnetic moment of a microparticle from the relaxation experiment in the air.[288,289] An extremely high magnetic field of 100 T was used for the phase transition studies.[290] Alternatively, the effect of the extremely low magnetic field of the Earth (<50 μT) was studied in relation to the mechanism of magnetoreception of bees, birds, and fishes.[291] Hore's group reported the radical-pair mechanism of light-sensitive cryptochrome proteins as a key reaction of magnetoreception,[292] but some researchers[293] proposed the role of magnetite in magnetoreception. Thus, the analytical applications of a geomagnetic field will be a fantastic future subject.

A magnetic gradient force was employed for the magnetophoretic velocity analysis of single microparticles, which attained attomole sensitivity for Mn(II). It is a unique advantage that the sensitivity of this method depends on the magnetic susceptibility of the analyte. Therefore, MNP can be recognized as an extremely sensitive tag in analyzing targeted bio-molecules and cells. When MNPs are used for migration or separation, the magnetic moment determined by the size and aggregation state of MNPs are crucially important, given that a single superparamagnetic MNP smaller than 10 nm is difficult to migrate in liquids by a magnetic gradient force. The study of dynamic force measurements by magnetic tweezers has been limited to DNA and proteins, but it should also be applied to the characterization of small molecules. Magneto-chromatography has not been improved to date, and thus substantial effort is required in the design of magnetic fields. The magneto-capillary effect, magnetic photonic crystals, and magnetic soft robots suggest valuable hints for future analytical applications.

Magnetic torque was utilized for the orientation of diamagnetic microcrystals by a static magnetic field and the alignment of microcrystals by a modulated magnetic field, which served for X-ray diffraction analysis.[187] The magnetic orientation of MNPs was studied by linear dichroism spectroscopy[205] and Sagnac interferometry.[294] Here, again, the aggregation state of MNPs will severely affect the interpretation of the observation. Optical polarization measurements of the magnetic orientation of MNPs will become a promising method to measure the viscosity of the nano-environment,[232] the stability of MNPs in solution, and the aggregation dynamics of nanoparticles given that the optical transition moment of MNPs is parallel to the easy axis

of the magnetic moment of MNP[295] and highly sensitive to the rotational relaxation dynamics.[228]

Electromagnetophoretic force was applied for the size separation and adsorption–desorption chromatography of microparticles,[238] but more applications should be investigated. The electromagnetophoretic buoyancy was shown to be useful for dynamic force measurement and manipulation of diamagnetic particles.[244] The local Lorentz force, which can be changed by the inhomogeneous current density around micro-subjects,[241,254] will be useful to fabricate micro-structured flow systems. In a Cu magneto-electrodeposition surface, its chiral selectivity was observed.[254] The chiral selectivity of the electrodeposited polymer and metal films needs to be studied more extensively. Alternatively, the contribution of electron spin orientation in the chiral molecule selectivity on ferromagnetic substrates was reported.[278] The role of electron spin in the adsorption and electrochemical reactions of chiral molecules is the hottest topic in magneto-electrochemistry given that it may bridge between spintronics and molecular chirality. Recently, chiral-induced spin selectivity in the formation and recombination of radical pairs in the cryptochrome magnetoreception was discussed.[296]

The migration and rotation of magnetic subjects were usually measured by microscopic, optical, and electrochemical methods. However, extremely sensitive magnetic sensors such as nitrogen-vacancy (NV) centers[297] and optically pumped magnetometers[298,299] have been developed and commercially available. These sensors will be applied in micro-analytical systems in the near future. In conclusion, we can say that the future of "magneto-analytical science" is very attractive.

Conflicts of interest

There are no conflicts of interest to declare.

Acknowledgements

This work was supported by JSPS KAKENHI grant numbers 21K05112 and 20K05551.

References

1 J. C. Giddings, *Unified Separation Science*, John Wiley & Sons, Ltd, New York, Chichester, Brisbane, Toronto, Singapore, 1991.
2 J. C. Giddings, *Anal. Chem.*, 1981, **53**, 945A–952A.
3 E. Maxwell, *Cryogenics*, 1975, **15**, 179–184.
4 M. Sagawa, S. Fujimura, H. Yamamoto, Y. Matsuura and K. Hiraga, *IEEE Trans. Magn.*, 1984, **20**, 1584–1589.
5 M. Hoenig, *IEEE Trans. Magn.*, 1983, **19**, 880–883.
6 J. M. D. Coey, *Magnetism and Magnetic Materials*, Cambridge University Press, Cambridge, 2010.
7 H. Watarai, M. Suwa and Y. Iiguni, *Anal. Bioanal. Chem.*, 2004, **378**, 1693–1699.
8 M. Suwa and H. Watarai, *Anal. Chim. Acta*, 2011, **690**, 137–147.
9 H. Watarai, *Annu. Rev. Anal. Chem.*, 2013, **6**, 353–378.
10 N. Pamme, *Lab Chip*, 2007, **7**, 1644–1659.
11 A. Munaz, M. J. A. Shiddiky and N.-T. Nguyen, *Biomicrofluidics*, 2018, **12**, 031501.
12 K. Aguilar-Arteaga, J. A. A. Rodriguez and E. Barrado, *Anal. Chim. Acta*, 2010, **674**, 157–165.
13 J. S. Beveridge, J. R. Stephens and M. E. Williams, *Annu. Rev. Anal. Chem.*, 2011, **4**, 251–273.
14 S. Wang, J. Xu, W. Li, S. Sun, S. Gao and Y. Hou, *Chem. Rev.*, 2022, **122**, 5411–5475.
15 A. van Reenen, A. M. de Jong, J. M. J. den Toonder and M. W. J. Prins, *Lab Chip*, 2014, **14**, 1966–1986.
16 K. R. Hurley, H. L. Ring, H. Kang, N. D. Klein and C. L. Haynes, *Anal. Chem.*, 2015, **87**, 11611–11619.
17 M. Faraji, *Nanochem. Res.*, 2016, **1**, 264–290.
18 C. P. Moerland, L. J. van IJzendoorn and M. W. J. Prins, *Lab Chip*, 2019, **19**, 919–933.
19 R. Soares, V. C. Martins, R. Macedo, F. A. Cardoso, S. A. M. Martins, D. M. Caetano, P. H. Fonseca, V. Silvério, S. Cardoso and P. P. Freitas, *Anal. Bioanal. Chem.*, 2019, **411**, 1839–1862.
20 X. Xuan, *Micromachines*, 2019, **10**, 744.
21 X. Liu, Y. Tian and L. Jiang, *Nano Lett.*, 2021, **21**, 2699–2708.
22 O. Civelekoglu, A. B. Frazier and A. F. Sarioglu, *Magnetochemistry*, 2022, **8**, 10.
23 T. B. Jones, *Electromechanisc of Particles*, Cambridge University Press, Cambridge, 1995.
24 S. J. Gill, C. P. Malone and M. Downing, *Rev. Sci. Instrum.*, 1960, **31**, 1299–1303.
25 M. Zborowski, C. B. Fuh, L. Sun, J. J. Chalmers and R. Green, *Anal. Chem.*, 1995, **67**, 3702–3712.
26 J. J. Chalmers, Y. Zhao, M. Nakamura, K. Melnik, L. Lasky, L. Moore and M. Zborowski, *J. Magn. Magn. Mater.*, 1999, **194**, 231–241.
27 J. J. Chalmers, S. Haam, Y. Zhao, K. McCloskey, L. Moore, M. Zborowski and P. S. Williams, *Biotechnol. Bioeng.*, 1999, **64**, 519–526.
28 M. Zborowski, G. R. Ostera, L. R. Moore, S. Milliron, J. J. Chalmers and A. N. Schechter, *Biophys. J.*, 2003, **84**, 2638–2645.
29 H. Zhang, L. R. Moore, M. Zborowski, P. S. Williams, S. Margel and J. J. Chalmers, *Analyst*, 2005, **130**, 514–527.
30 E. J. Chosy, M. Nakamura, K. Melnik, K. Comella, L. C. Lasky, M. Zborowski and J. J. Chalmers, *Biotechnol. Bioeng.*, 2003, **82**, 340–351.
31 D. R. Leigh, S. Steinert, L. R. Moore, J. J. Chalmers and M. Zborowski, *Cytometry, Part A*, 2005, **66**, 103–108.
32 X. Jin, Y. Zhao, A. Richardson, L. Moore, P. S. Williams, M. Zborowski and J. J. Chalmers, *Analyst*, 2008, **133**, 1767.
33 W. Xue, L. R. Moore, N. Nakano, J. J. Chalmers and M. Zborowski, *J. Magn. Magn. Mater.*, 2019, **474**, 152–160.
34 J. Kim, J. Gómez-Pastora, M. Weigand, M. Potgieter, N. A. Walters, E. Reátegui, A. F. Palmer, M. Yazer, M. Zborowski and J. J. Chalmers, *Cytometry, Part A*, 2019, **95**, 478–487.

35 J. Gómez-Pastora, J. Kim, V. Multanen, M. Weigand, N. A. Walters, E. Reátegui, A. F. Palmer, M. H. Yazer, M. Zborowski and J. J. Chalmers, *Exp. Hematol.*, 2021, **99**, 21–31, e5.
36 J. Kim, M. Weigand, A. F. Palmer, M. Zborowski, M. H. Yazer and J. J. Chalmers, *Analyst*, 2019, **144**, 935–942.
37 M. R. H. Weigand, J. Gómez-Pastora, J. Kim, M. T. Kurek, R. J. Hickey, D. C. Irwin, P. W. Buehler, M. Zborowski, A. F. Palmer and J. J. Chalmers, *PLoS One*, 2021, **16**, 1–14.
38 X. Jin, J. J. Chalmers and M. Zborowski, *Anal. Chem.*, 2012, **84**, 4520–4526.
39 J. Kim, J. Gómez-Pastora, C. J. Gilbert, M. Weigand, N. A. Walters, E. Reátegui, A. F. Palmer, M. Yazer, M. Zborowski and J. J. Chalmers, *Anal. Chem.*, 2020, **92**, 1956–1962.
40 J. Gómez-Pastora, M. Weigand, J. Kim, A. F. Palmer, M. Yazer, P. C. Desai, M. Zborowski and J. J. Chalmers, *Sci. Rep.*, 2022, **12**, 1–12.
41 X. Jin, M. H. Yazer, J. J. Chalmers and M. Zborowski, *Analyst*, 2011, **136**, 2996.
42 J. J. Chalmers, X. Jin, A. F. Palmer, M. H. Yazer, L. Moore, P. Amaya, K. Park, X. Pan and M. Zborowski, *Anal. Chem.*, 2017, **89**, 3702–3709.
43 H. Watarai and M. Namba, *Anal. Sci.*, 2001, **17**, 1233–1236.
44 M. Suwa and H. Watarai, *Anal. Chem.*, 2002, **74**(19), 5027–5032.
45 M. Suwa and H. Watarai, *J. Chromatogr. A*, 2003, **1013**, 3–8.
46 M. Suwa and H. Watarai, *Anal. Sci.*, 2008, **24**, 133–137.
47 N. Shimamoto, S. Ohkoshi, O. Sato and K. Hashimoto, *Chem. Lett.*, 2002, **31**, 486–487.
48 N. Shimamoto, S. Ohkoshi, O. Sato and K. Hashimoto, *Inorg. Chem.*, 2002, **41**, 678–684.
49 M. Suwa and H. Watarai, *Chem. Commun.*, 2004, 1656.
50 M. Suwa and H. Watarai, *Sci. Technol. Adv. Mater.*, 2006, **7**, 373–379.
51 S. Egami and H. Watarai, *Analyst*, 2009, **134**, 278–282.
52 Y. Urabe, H. Monjushiro and H. Watarai, *AIP Adv.*, 2020, **10**, 2–5.
53 H. Watarai and J. Chen, *Anal. Chem.*, 2017, **89**, 10141–10146.
54 H. Watarai and M. Kurahashi, *Anal. Chim. Acta*, 2020, **1111**, 60–66.
55 M. Kawano and H. Watarai, *Analyst*, 2012, **137**, 4123.
56 H. Watarai, H. T. T. Duc, T. T. N. Lan, T. Zhang and S. Tsukahara, *Anal. Sci.*, 2014, **30**, 745–749.
57 J. Lim, C. Lanni, E. R. Evarts, F. Lanni, R. D. Tilton and S. A. Majetich, *ACS Nano*, 2011, **5**, 217–226.
58 P. Zhang, S. Park and S. H. Kang, *Chem. Commun.*, 2013, **49**, 7298.
59 S. S. Leong, Z. Ahmad, S. C. Low, J. Camacho, J. Faraudo and J. Lim, *Langmuir*, 2020, **36**, 8033–8055.
60 J. Faraudo, J. S. Andreu and J. Camacho, *Soft Matter*, 2013, **9**, 6654.
61 J. S. Andreu, J. Camacho, J. Faraudo, M. Benelmekki, C. Rebollo and L. M. Martínez, *Phys. Rev. E: Stat., Nonlinear, Soft Matter Phys.*, 2011, **84**, 1–8.
62 S. S. Leong, Z. Ahmad and J. Lim, *Soft Matter*, 2015, **11**, 6968–6980.
63 Y. Ikezoe, N. Hirota, J. Nakagawa and K. Kitazawa, *Nature*, 1998, **393**, 749–750.
64 Y. Ikezoe, T. Kaihatsu, S. Sakae, H. Uetake, N. Hirota and K. Kitazawa, *Energy Convers. Manage.*, 2002, **43**, 417–425.
65 H. Watarai and M. Namba, *J. Chromatogr. A*, 2002, **961**, 3–8.
66 S. Ge, A. Nemiroski, K. A. Mirica, C. R. Mace, J. W. Hennek, A. A. Kumar and G. M. Whitesides, *Angew. Chem., Int. Ed*, 2020, **59**, 17810–17855.
67 A. Winkleman, R. Perez-Castillejos, K. L. Gudiksen, S. T. Phillips, M. Prentiss and G. M. Whitesides, *Anal. Chem.*, 2007, **79**, 6542–6550.
68 K. A. Mirica, S. T. Phillips, C. R. MacE and G. M. Whitesides, *J. Agric. Food Chem.*, 2010, **58**, 6565–6569.
69 M. B. J. Atkinson, D. K. Bwambok, J. Chen, P. D. Chopade, M. M. Thuo, C. R. Mace, K. A. Mirica, A. A. Kumar, A. S. Myerson and G. M. Whitesides, *Angew. Chem., Int. Ed.*, 2013, **52**, 10208–10211.
70 C. K. Abrahamsson, A. Nagarkar, M. J. Fink, D. J. Preston, S. Ge, J. S. Bozenko and G. M. Whitesides, *Angew. Chem., Int. Ed.*, 2020, **59**, 874–881.
71 A. I. Rodríguez-Villarreal, M. D. Tarn, L. A. Madden, J. B. Lutz, J. Greenman, J. Samitier and N. Pamme, *Lab Chip*, 2011, **11**, 1240–1248.
72 J. Nguyen, D. V. Conca, J. Stein, L. Bovo, C. A. Howard and I. Llorente Garcia, *Proc. Natl. Acad. Sci. U. S. A.*, 2019, **116**, 2425–2434.
73 P. Dunne, T. Adachi, A. A. Dev, A. Sorrenti, L. Giacchetti, A. Bonnin, C. Bourdon, P. H. Mangin, J. M. D. Coey, B. Doudin and T. M. Hermans, *Nature*, 2020, **581**, 58–62.
74 B. Ngamsom, E. A. Wandera, A. Iles, R. Kimani, F. Muregi, J. Gitaka and N. Pamme, *Analyst*, 2019, **144**, 6889–6897.
75 F. Shen, H. Hwang, Y. K. Hahn and J. K. Park, *Anal. Chem.*, 2012, **84**, 3075–3081.
76 Y. Jo, Y. K. Hahn and J. K. Park, *Microfluid. Nanofluid.*, 2017, **21**, 1–11.
77 F. Shen and J. K. Park, *Anal. Chem.*, 2018, **90**, 920–927.
78 G. P. Zhu, M. Hejiazan, X. Huang and N. T. Nguyen, *Lab Chip*, 2014, **14**, 4609–4615.
79 Z. D. Call, C. S. Carrell, I. Jang, B. J. Geiss, D. S. Dandy and C. S. Henry, *Anal. Methods*, 2020, **12**, 5177–5185.
80 N. Pamme and A. Manz, *Anal. Chem.*, 2004, **76**, 7250–7256.
81 A. Q. Alorabi, M. D. Tarn, J. Gómez-Pastora, E. Bringas, I. Ortiz, V. N. Paunov and N. Pamme, *Lab Chip*, 2017, **17**, 3785–3795.
82 M. Navi, N. Abbasi, M. Jeyhani, V. Gnyawali and S. S. H. Tsai, *Lab Chip*, 2018, **18**, 3361–3370.
83 K. Zhang, Q. Liang, X. Ai, P. Hu, Y. Wang and G. Luo, *Anal. Chem.*, 2011, **83**, 8029–8034.
84 C. W. Shields IV, J. L. Wang, K. A. Ohiri, E. D. Essoyan, B. B. Yellen, A. J. Armstrong and G. P. López, *Lab Chip*, 2016, **16**, 3833–3844.
85 K. Choi, A. H. C. Ng, R. Fobel and A. R. Wheeler, *Annu. Rev. Anal. Chem.*, 2012, **5**, 413–440.

86 Z.-G. Guo, W.-M. Liu and B.-L. Su, *Appl. Phys. Lett.*, 2008, **92**, 063104.
87 R. P. S. De Campos, D. G. Rackus, R. Shih, C. Zhao, X. Liu and A. R. Wheeler, *Anal. Chem.*, 2019, **91**, 2506–2515.
88 C. Dixon, J. Lamanna and A. R. Wheeler, *Lab Chip*, 2020, **20**, 1845–1855.
89 T. Narahari, J. Dahmer, A. Sklavounos, T. Kim, M. Satkauskas, I. Clotea, M. Ho, J. Lamanna, C. Dixon, D. G. Rackus, S. J. R. da Silva, L. Pena, K. Pardee and A. R. Wheeler, *Lab Chip*, 2022, **22**, 1748–1763.
90 T. J. Hutama and R. D. Oleschuk, *Lab Chip*, 2017, **17**, 2640–2649.
91 P. Agrawal, K. J. Bachus, G. Carriere, P. Grouse and R. D. Oleschuk, *Anal. Bioanal. Chem.*, 2019, **411**, 5393–5403.
92 S. B. Smith, L. Finzi and C. Bustamante, *Science*, 1992, **258**, 1122–1126.
93 T. R. Strick, J. F. Allemand, D. Bensimon, A. Bensimon and V. Croquette, *Science*, 1996, **271**, 1835–1837.
94 C. Haber and D. Wirtz, *Rev. Sci. Instrum.*, 2000, **71**, 4561.
95 C. Gosse and V. Croquette, *Biophys. J.*, 2002, **82**, 3314–3329.
96 I. Vilfan, B. Startup, J. Lipfert, D. A. Koster and N. Dekker, *Handbook of Single-Molecule Biophysics*, Springer, US, New York, NY, 2009.
97 X. Zhang, H. Chen, H. Fu, P. S. Doyle and J. Yan, *Proc. Natl. Acad. Sci. U. S. A.*, 2012, **109**, 8103–8108.
98 Y.-J. Yang, H.-L. Dong, X.-W. Qiang, H. Fu, E.-C. Zhou, C. Zhang, L. Yin, X.-F. Chen, F.-C. Jia, L. Dai, Z.-J. Tan and X.-H. Zhang, *J. Am. Chem. Soc.*, 2020, **142**, 9203–9209.
99 E. Evans, *Annu. Rev. Biophys. Biomol. Struct.*, 2001, **30**, 105–128.
100 V. Vogel, *Annu. Rev. Biophys. Biomol. Struct.*, 2006, **35**, 459–488.
101 M. Kruithof, F. Chien, M. De Jager and J. Van Noort, *Biophys. J.*, 2008, **94**, 2343–2348.
102 T. Goto and H. Watarai, *Langmuir*, 2010, **26**, 4848–4853.
103 G. Y. Yu, W. D. Hunt, M. Josowicz and J. Janata, *Rev. Sci. Instrum.*, 2007, **78**, 065111.
104 S. Imai and H. Watarai, *Anal. Sci.*, 2012, **28**, 833–836.
105 D. Vella and L. Mahadevan, *Am. J. Phys.*, 2005, **73**, 817–825.
106 N. Vandewalle, L. Clermont, D. Terwagne, S. Dorbolo, E. Mersch and G. Lumay, *Phys. Rev. E: Stat., Nonlinear, Soft Matter Phys.*, 2012, **85**, 041402.
107 N. Vandewalle, N. Obara and G. Lumay, *Eur. Phys. J. E: Soft Matter Biol. Phys.*, 2013, **36**, 127.
108 W. Fei, M. M. Driscoll, P. M. Chaikin and K. J. M. Bishop, *Soft Matter*, 2018, **14**, 4661–4665.
109 F. Liu, Y. Li, Y. Huang, A. Tsyrenova, K. Miller, L. Zhou, H. Qin and S. Jiang, *Nano Lett.*, 2020, **20**, 8773–8780.
110 W. Fei, P. M. Tzelios and K. J. M. Bishop, *Langmuir*, 2020, **36**, 6977–6983.
111 S. Ghosh, T. H. Fang, M. S. Uddin and K. Hidajat, *Colloids Surf., B*, 2013, **105**, 267–277.
112 R. Kaur, P. Khullar, A. Gupta and M. S. Bakshi, *Langmuir*, 2021, **37**, 14558–14570.
113 L.-L. Wu, M. Tang, Z.-L. Zhang, C.-B. Qi, J. Hu, X.-Y. Ma and D.-W. Pang, *Anal. Chem.*, 2018, **90**, 10518–10526.
114 S.-L. Hong, Y.-N. Zhang, Y.-H. Liu, M. Tang, D.-W. Pang, G. Wong, J. Chen, X. Qiu, G. F. Gao, W. Liu, Y. Bi and Z.-L. Zhang, *Anal. Chem.*, 2018, **90**, 7310–7317.
115 H. Y. Tsai, S. Y. Li and C. B. Fuh, *Anal. Bioanal. Chem.*, 2018, **410**, 1923–1929.
116 Q. Zhang, Y. Huang, B. Jiang, Y. Hu, J. Xie, X. Gao, B. Jia, H. Shen, W. Zhang and P. Yang, *Anal. Chem.*, 2018, **90**, 7357–7363.
117 H. Zhang, H. Lai, X. Wu, G. Li and Y. Hu, *Anal. Chem.*, 2020, **92**, 4607–4613.
118 J. Kang, D. Kang, G. Yeom and C.-J. Park, *Anal. Chem.*, 2021, **93**, 16804–16812.
119 A. Bagheri, M. Taghizadeh, M. Behbahani, A. Akbar Asgharinezhad, M. Salarian, A. Dehghani, H. Ebrahimzadeh and M. M. Amini, *Talanta*, 2012, **99**, 132–139.
120 M. Esmaeilzadeh, *Microchim. Acta*, 2019, **186**, 14.
121 L. Huang, M. He, B. Chen and B. Hu, *J. Mater. Chem. A*, 2015, **3**, 11587–11595.
122 S. Rezabeyk and M. Manoochehri, *RSC Adv.*, 2020, **10**, 36897–36905.
123 M. Zhao, C. Deng, X. Zhang and P. Yang, *Proteomics*, 2013, **13**, 3387–3392.
124 J.-P. Wei, H. Wang, T. Luo, Z.-J. Zhou, Y.-F. Huang and B. Qiao, *Anal. Bioanal. Chem.*, 2017, **409**, 1895–1904.
125 Y. Xu, J. Jin, X. Li, Y. Han, H. Meng, C. Song and X. Zhang, *Microchim. Acta*, 2015, **182**, 2313–2320.
126 Y. Xu, J. Jin, X. Li, Y. Han, H. Meng, J. Wu and X. Zhang, *J. Sep. Sci.*, 2016, **39**, 3647–3654.
127 N. Zhang, N. Sun and C. Deng, *Chem. Commun.*, 2020, **56**, 13999–14002.
128 K. D. Clark, M. N. Emaus, M. Varona, A. N. Bowers and J. L. Anderson, *J. Sep. Sci.*, 2018, **41**, 209–235.
129 S. A. Pierson, O. Nacham, K. D. Clark, H. Nan, Y. Mudryk and J. L. Anderson, *New J. Chem.*, 2017, **41**, 5498–5505.
130 M. A. Abdelaziz, F. R. Mansour and N. D. Danielson, *Anal. Bioanal. Chem.*, 2021, **413**, 205–214.
131 E. Fernández, L. Vidal and A. Canals, *Anal. Bioanal. Chem.*, 2018, **410**, 4679–4687.
132 J. Merib, D. A. Spudeit, G. Corazza, E. Carasek and J. L. Anderson, *Anal. Bioanal. Chem.*, 2018, **410**, 4689–4699.
133 K. D. Clark, J. A. Purslow, S. A. Pierson, O. Nacham and J. L. Anderson, *Anal. Bioanal. Chem.*, 2017, **409**, 4983–4991.
134 K. D. Clark, O. Nacham, H. Yu, T. Li, M. M. Yamsek, D. R. Ronning and J. L. Anderson, *Anal. Chem.*, 2015, **87**, 1552–1559.
135 X. Wang, M. Liu and X. Ding, *Langmuir*, 2021, **37**, 11665–11675.
136 A. Marengo, M. N. Emaus, C. M. Bertea, C. Bicchi, P. Rubiolo, C. Cagliero and J. L. Anderson, *Anal. Bioanal. Chem.*, 2019, **411**, 6583–6590.
137 A. N. Bowers, M. J. Trujillo-Rodríguez, M. Q. Farooq and J. L. Anderson, *Anal. Bioanal. Chem.*, 2019, **411**, 7375–7385.
138 M. N. Emaus and J. L. Anderson, *Anal. Bioanal. Chem.*, 2020, **412**, 8039–8049.
139 M. N. Emaus, K. D. Clark, P. Hinners and J. L. Anderson, *Anal. Bioanal. Chem.*, 2018, **410**, 4135–4144.

140 S. Tsukahara, A. Takata and H. Watarai, *Anal. Sci.*, 2004, **20**, 1515–1521.
141 A. Takata, S. Tsukahara and H. Watarai, *Chem. Lett.*, 2004, **33**, 518–519.
142 H. Y. Tsai, C. Yin, Y. P. Lin and C. B. Fuh, *J. Chromatogr. A*, 2006, **1120**, 35–37.
143 H. Y. Tsai, C. F. Hsu, I. W. Chiu and C. Bor Fuh, *Anal. Chem.*, 2007, **79**, 8416–8419.
144 H. Y. Tsai, J. R. Chan, Y. C. Li, F. C. Cheng and C. B. Fuh, *Biosens. Bioelectron.*, 2010, **25**, 2701–2705.
145 C. S. Li, S. H. Chen, H. Y. Tsai and C. B. Fuh, *Sens. Actuators, B*, 2012, **166–167**, 819–823.
146 H. Y. Tsai, M. J. Chuang, B. C. Chou, S. F. Yang and C. Bor Fuh, *Sens. Actuators, B*, 2016, **223**, 834–838.
147 H. G. Mukherjee, D. Majumder and N. K. Srimani, *J. Indian Chem. Soc.*, 1980, **11**, 939–941.
148 T. Nomizu, K. Yamamoto and M. Watanabe, *Anal. Sci.*, 2001, **17**, 177–180.
149 M. Fujiwara, D. Kodoi, W. Duan and Y. Tanimoto, *J. Phys. Chem. B*, 2001, **105**, 3343–3345.
150 M. Fujiwara, K. Chie, J. Sawai, D. Shimizu and Y. Tanimoto, *J. Phys. Chem. B*, 2004, **108**, 3531–3534.
151 M. Fujiwara, K. Mitsuda and Y. Tanimoto, *J. Phys. Chem. B*, 2006, **110**, 13965–13969.
152 E. Barrado and J. A. Rodríguez, *J. Chromatogr. A*, 2006, **1128**, 189–193.
153 Z. Cai, N. L. Smith, J.-T. Zhang and S. A. Asher, *Anal. Chem.*, 2015, **87**, 5013–5025.
154 H. Hu, C. Chen and Q. Chen, *J. Mater. Chem. C*, 2013, **1**, 6013.
155 J. Ge, Y. Hu and Y. Yin, *Angew. Chem., Int. Ed.*, 2007, **46**, 7428–7431.
156 R. Xuan, Q. Wu, Y. Yin and J. Ge, *J. Mater. Chem.*, 2011, **21**, 3672–3676.
157 H. Hu, H. Zhong, C. Chen and Q. Chen, *J. Mater. Chem. C*, 2014, **2**, 3695.
158 M. Zhang, D. J. Magagnosc, I. Liberal, Y. Yu, H. Yun, H. Yang, Y. Wu, J. Guo, W. Chen, Y. J. Shin, A. Stein, J. M. Kikkawa, N. Engheta, D. S. Gianola, C. B. Murray and C. R. Kagan, *Nat. Nanotechnol.*, 2017, **12**, 228–232.
159 V. T. Tran, D. K. Lee, J. Kim, K.-J. Jeong, C.-S. Kim and J. Lee, *ACS Appl. Mater. Interfaces*, 2020, **12**, 16584–16591.
160 Y. Kim and X. Zhao, *Chem. Rev.*, 2022, **122**, 5317–5364.
161 X. Zhao, J. Kim, C. A. Cezar, N. Huebsch, K. Lee, K. Bouhadir and D. J. Mooney, *Proc. Natl. Acad. Sci. U. S. A.*, 2011, **108**, 67–72.
162 J. Zhang, Z. Ren, W. Hu, R. H. Soon, I. C. Yasa, Z. Liu and M. Sitti, *Sci. Robot.*, 2021, **6**, eabf0112.
163 R. María-Hormigos, B. Jurado-Sánchez and A. Escarpa, *Anal. Chem.*, 2018, **90**, 9830–9837.
164 J. Yu, D. Jin, K.-F. Chan, Q. Wang, K. Yuan and L. Zhang, *Nat. Commun.*, 2019, **10**, 5631.
165 Q. Wang, K. F. Chan, K. Schweizer, X. Du, D. Jin, S. C. H. Yu, B. J. Nelson and L. Zhang, *Sci. Adv.*, 2021, **7**, 1–13.
166 B. Wang, K. F. Chan, K. Yuan, Q. Wang, X. Xia, L. Yang, H. Ko, Y.-X. J. Wang, J. J. Y. Sung, P. W. Y. Chiu and L. Zhang, *Sci. Robot.*, 2021, **6**, eabd2813.
167 D. Jin and L. Zhang, *Acc. Chem. Res.*, 2022, **55**, 98–109.
168 T. Takeuchi, T. Mizuno, T. Higashi, A. Yamagishi and M. Date, *J. Magn. Magn. Mater.*, 1995, **140–144**, 1462–1463.
169 T. Takeuchi, T. Mizuno, T. Higashi, A. Yamagishi and M. Date, *Phys. B*, 1994, **201**, 601–605.
170 T. Higashi, A. Yamagishi, T. Takeuchi, N. Kawaguchi, S. Sagawa, S. Onishi and M. Date, *Blood*, 1993, **82**, 1328–1334.
171 Y. Kitahama, Y. Kimura and K. Takazawa, *Langmuir*, 2006, **22**, 7600–7604.
172 Y. Fujiwara, N. Shibata, Y. Matsumoto and Y. Tanimoto, *J. Magn. Magn. Mater.*, 2007, **310**, 2859–2861.
173 H. Yonemura, Y. Yamamoto, S. Yamada, Y. Fujiwara and Y. Tanimoto, *Sci. Technol. Adv. Mater.*, 2008, **9**, 024213.
174 H. Yonemura, K. Yuno, Y. Yamamoto, S. Yamada, Y. Fujiwara and Y. Tanimoto, *Synth. Met.*, 2009, **159**, 955–960.
175 H. Yonemura, K. Yuno and S. Yamada, *Jpn. J. Appl. Phys.*, 2010, **49**, 01AE06.
176 H. Yonemura, J. Suyama, T. Arakawa and S. Yamada, *Thin Solid Films*, 2009, **518**, 668–673.
177 H. Yonemura, S. Natsuko, J. Suyama and S. Yamada, *J. Photochem. Photobiol., A*, 2011, **220**, 179–187.
178 Y. Takeuchi, Y. Sugawara, T. Sugawara and M. Iwasaka, *IEEE Trans. Magn.*, 2014, **50**, 1–4.
179 Y. Takeuchi, M. Sekiya, A. Hamasaki, M. Iwasaka and M. Matsuda, *IEEE Trans. Magn.*, 2017, **57**, 5100105.
180 Y. Takeuchi, M. Iwasaka, M. Matsuda and A. Hamasaki, *IEEE Trans. Magn.*, 2021, **57**, 1–5.
181 M. Iwasaka and Y. Mizukawa, *Langmuir*, 2013, **29**, 4328–4334.
182 M. Iwasaka, Y. Mizukawa and N. W. Roberts, *Langmuir*, 2016, **32**, 180–187.
183 P. G. de Gennes and J. Prost, *The Physics of Liquid Crystals*, Oxford University Press, Oxford, 2nd edn, 1993.
184 Y.-K. Kim, J. Noh, K. Nayani and N. L. Abbott, *Soft Matter*, 2019, **15**, 6913–6929.
185 N. L. Abbott, Eng. Sci. Fundam. - Core Program. Top. 2011 AIChE Annu. Meet., 2011, 1, pp. 27–28.
186 F. Yesil, M. Suwa and S. Tsukahara, *Langmuir*, 2018, **34**, 81–87.
187 T. Kimura and M. Yoshino, *Langmuir*, 2005, **21**, 4805–4808.
188 M. Yamaguchi, S. Ozawa and I. Yamamoto, *Jpn. J. Appl. Phys.*, 2010, **49**, 6–9.
189 M. Yamaguchi, I. Yamamoto and T. Kimura, *Jpn. J. Appl. Phys.*, 2013, **52**, 6–9.
190 F. Kimura, W. Oshima, H. Matsumoto, H. Uekusa, K. Aburaya, M. Maeyama and T. Kimura, *CrystEngComm*, 2014, **16**, 6630–6634.
191 F. Kimura, T. Kimura, W. Oshima, M. Maeyama and K. Aburaya, *J. Appl. Crystallogr.*, 2010, **43**, 151–153.
192 T. Kimura, C. Chang, F. Kimura and M. Maeyama, *J. Appl. Crystallogr.*, 2009, **42**, 535–537.
193 F. Kimura, K. Mizutani, B. Mikami and T. Kimura, *Cryst. Growth Des.*, 2011, **11**, 12–15.
194 S. Tsukui, F. Kimura, E. F. Garman, S. Baba, N. Mizuno, B. Mikami and T. Kimura, *J. Appl. Crystallogr.*, 2016, **49**, 457–461.

195 S. Tsukui, F. Kimura, K. Kusaka, S. Baba, N. Mizuno and T. Kimura, *Acta Crystallogr., Sect. D: Struct. Biol.*, 2016, **72**, 823–829.
196 R. Kusumi, F. Kimura, G. Song and T. Kimura, *J. Magn. Reson.*, 2012, **223**, 68–72.
197 F. Kimura and T. Kimura, *CrystEngComm*, 2018, **20**, 861–872.
198 C. Tsuboi, K. Aburaya, F. Kimura, M. Maeyama and T. Kimura, *CrystEngComm*, 2016, **18**, 2404–2407.
199 C. Tsuboi, S. Tsukui, F. Kimura, T. Kimura, K. Hasegawa, S. Baba and N. Mizuno, *J. Appl. Crystallogr.*, 2016, **49**, 2100–2105.
200 C. Tsuboi, F. Kimura, T. Tanaka and T. Kimura, *Cryst. Growth Des.*, 2016, **16**, 2810–2813.
201 J. P. Llewellyn, *J. Phys. D: Appl. Phys.*, 1983, **16**, 95.
202 M. Xu and P. J. Ridler, *J. Appl. Phys.*, 1997, **82**, 326–332.
203 F. Bentivegna, J. Ferré, M. Nývlt, J. P. Jamet, D. Imhoff, M. Canva, A. Brun, P. Veillet, Š. Višňovský, F. Chaput and J. P. Boilot, *J. Appl. Phys.*, 1998, **83**, 7776–7788.
204 E. Hasmonay, E. Dubois, S. Neveu, J. C. Bacri and R. Perzynski, *Eur. Phys. J. B*, 2001, **21**, 19–29.
205 H. Watarai and S. S. M. Sakurai, *Langmuir*, 2020, **36**, 12414–12422.
206 G. Trefalt, I. Szilagyi, T. Oncsik, A. Sadeghpour and M. Borkovec, *Chimia*, 2013, **67**, 772.
207 A. Ranzoni, J. J. H. B. Schleipen, L. J. van IJzendoorn and M. W. J. Prins, *Nano Lett.*, 2011, **11**, 2017–2022.
208 A. Ranzoni, G. Sabatte, L. J. van IJzendoorn and M. W. J. Prins, *ACS Nano*, 2012, **6**, 3134–3141.
209 F. A. Gutiérrez-Mejiá, C. P. Moerland, L. J. Van Ijzendoorn and M. W. J. Prins, *Nanoscale*, 2019, **11**, 19933–19942.
210 M. R. W. Scheepers, A. R. Romijn, L. J. Van Ijzendoorn and M. W. J. Prins, *Langmuir*, 2019, **35**, 10533–10541.
211 M. R. W. Scheepers, S. R. R. Haenen, J. M. Coers, L. J. van IJzendoorn and M. W. J. Prins, *Nanoscale*, 2020, **12**, 14605–14614.
212 B. Gleich and J. Weizenecker, *Nature*, 2005, **435**, 1214–1217.
213 E. Y. Yu, M. Bishop, B. Zheng, R. M. Ferguson, A. P. Khandhar, S. J. Kemp, K. M. Krishnan, P. W. Goodwill and S. M. Conolly, *Nano Lett.*, 2017, **17**, 1648–1654.
214 F. J. Teran, C. Casado, N. Mikuszeit, G. Salas, A. Bollero, M. P. Morales, J. Camarero and R. Miranda, *Appl. Phys. Lett.*, 2012, **101**, 62413.
215 D. Cabrera, A. Coene, J. Leliaert, E. J. Artés-Ibáñez, L. Dupré, N. D. Telling and F. J. Teran, *ACS Nano*, 2018, **12**, 2741–2752.
216 M. Hess, E. Roeben, A. Habicht, S. Seiffert and A. M. Schmidt, *Soft Matter*, 2019, **15**, 842–850.
217 A. C. Bohórquez, M. Unni, S. Belsare, A. Chiu-Lam, L. Rice, C. Pampo, D. Siemann and C. Rinaldi, *Bioconjugate Chem.*, 2018, **29**, 2793–2805.
218 M. Hess, M. Gratz, H. Remmer, S. Webers, J. Landers, D. Borin, F. Ludwig, H. Wende, S. Odenbach, A. Tschöpe and A. M. Schmidt, *Soft Matter*, 2020, **16**, 7562–7575.
219 M. Donolato, P. Antunes, R. S. Bejhed, T. Zardán Gómez de la Torre, F. W. Østerberg, M. Strömberg, M. Nilsson, M. Strømme, P. Svedlindh, M. F. Hansen and P. Vavassori, *Anal. Chem.*, 2015, **87**, 1622–1629.
220 B. Tian, J. Fock, G. A. S. Minero, F. Garbarino and M. F. Hansen, *Anal. Chem.*, 2019, **91**, 10102–10109.
221 J. Carrey, B. Mehdaoui and M. Respaud, *J. Appl. Phys.*, 2011, **109**, 83921.
222 N. A. Usov and B. Y. Liubimov, *J. Appl. Phys.*, 2012, **112**, 23901.
223 S. Ota, Y. Matsugi, T. Nakamura, R. Takeda, Y. Takemura, I. Kato, S. Nohara, T. Sasayama, T. Yoshida and K. Enpuku, *J. Magn. Magn. Mater.*, 2019, **474**, 311–318.
224 H. Mamiya and B. Jeyadevan, *Sci. Rep.*, 2011, **1**, 157.
225 S. A. Shah, D. B. Reeves, R. M. Ferguson, J. B. Weaver and K. M. Krishnan, *Phys. Rev. B: Condens. Matter Mater. Phys.*, 2015, **92**, 94438.
226 S. B. Trisnanto, S. Ota and Y. Takemura, *Appl. Phys. Express*, 2018, **11**, 75001.
227 L. M. Bauer, S. F. Situ, M. A. Griswold and A. C. S. Samia, *J. Phys. Chem. Lett.*, 2015, **6**, 2509–2517.
228 S. Ota and Y. Takemura, *J. Phys. Chem. C*, 2019, **123**, 28859–28866.
229 M. Suwa and H. Watarai, *J. Phys.: Conf. Ser.*, 2009, **156**, 012025.
230 M. Suwa, A. Uotani and S. Tsukahara, *J. Appl. Phys.*, 2019, **125**, 123901.
231 M. Suwa, A. Uotani and S. Tsukahara, *Appl. Phys. Lett.*, 2020, **116**, 262403.
232 M. Suwa, A. Uotani, Y. Tojo, R. Onodera and S. Tsukahara, *Langmuir*, 2022, **38**, 9708–9719.
233 A. Kolin, *Science*, 1953, **117**, 134–137.
234 A. Kolin and R. T. Kado, *Nature*, 1958, **182**, 510–512.
235 S. Ozawa, D. Kurosaka, I. Yamamoto and T. Takamasu, *Jpn. J. Appl. Phys.*, 2011, **50**, 070212.
236 M. Namba, H. Watarai and T. Takeuchi, *Anal. Sci.*, 2000, **16**, 5–9.
237 Y. Iiguni and H. Ohtani, *Anal. Sci.*, 2013, **29**, 35–39.
238 Y. Iiguni and H. Watarai, *J. Chromatogr. A*, 2005, **1073**, 93–98.
239 Y. Fukui, Y. Iiguni, S. Kitagawa and H. Ohtani, *Anal. Sci.*, 2015, **31**, 197–203.
240 Y. Iiguni, A. Tanaka, S. Kitagawa and H. Ohtani, *Anal. Sci.*, 2016, **32**, 41–48.
241 M. Funaki, M. Suwa and H. Watarai, *Anal. Sci.*, 2017, **33**, 1013–1019.
242 Y. Iiguni and H. Watarai, *Anal. Sci.*, 2003, **19**, 33–37.
243 Y. Iiguni and H. Watarai, *Bull. Chem. Soc. Jpn.*, 2006, **79**, 47–52.
244 Y. Iiguni and H. Watarai, *Analyst*, 2010, **135**, 1426–1432.
245 T. Kato, Y. Iiguni and H. Watarai, *Bull. Chem. Soc. Jpn.*, 2016, **89**, 1487–1492.
246 G. I. Bell, *Science*, 1978, **200**, 618–627.
247 S. Wakiyama and H. Watarai, *Anal. Sci.*, 2017, **33**, 399–401.
248 L. M. A. Monzon and J. M. D. Coey, *Electrochem. Commun.*, 2014, **42**, 38–41.
249 R. Aogaki, K. Fueki and T. Mukaibo, *Denki Kagaku oyobi Kogyo Butsuri Kagaku*, 1975, **43**, 504–508.

250 R. Aogaki, R. Morimoto and M. Asanuma, *J. Magn. Magn. Mater.*, 2010, **322**, 1664–1668.
251 R. Morimoto, M. Miura, A. Sugiyama, M. Miura, Y. Oshikiri, Y. Kim, I. Mogi, S. Takagi, Y. Yamauchi and R. Aogaki, *J. Phys. Chem. B*, 2020, **124**, 11854–11869.
252 R. Morimoto, M. Miura, A. Sugiyama, M. Miura, Y. Oshikiri, Y. Kim, I. Mogi, S. Takagi, Y. Yamauchi and R. Aogaki, *J. Phys. Chem. B*, 2020, **124**, 11870–11881.
253 R. Aogaki, *Magnetohydrodynamics*, 2003, **39**, 453–460.
254 I. Mogi, R. Morimoto, R. Aogaki and K. Watanabe, *Sci. Rep.*, 2013, **3**, 2574.
255 I. Mogi, R. Morimoto and R. Aogaki, *Curr. Opin. Electrochem.*, 2018, **7**, 1–6.
256 M. Huang, K. Skibinska, P. Zabinski, M. Wojnicki, G. Włoch, K. Eckert and G. Mutschke, *Electrochim. Acta*, 2022, **420**, 140422.
257 G. Mutschke, K. Tschulik, T. Weier, M. Uhlemann, A. Bund and J. Fröhlich, *Electrochim. Acta*, 2010, **55**, 9060–9066.
258 G. Mutschke, K. Tschulik, M. Uhlemann, A. Bund and J. Fröhlich, *Phys. Rev. Lett.*, 2012, **109**, 229401.
259 I. Mogi, R. Aogaki, R. Morimoto and K. Watanabe, *Acta Phys. Pol., A*, 2014, **126**, 380–381.
260 N. Leventis and X. Gao, *Anal. Chem.*, 2001, **73**, 3981–3992.
261 J. West, B. Karamata, B. Lillis, J. P. Gleeson, J. Alderman, J. K. Collins, W. Lane, A. Mathewson and H. Berney, *Lab Chip*, 2002, **2**, 224–230.
262 S. Qian and H. H. Bau, *Mech. Res. Commun.*, 2009, **36**, 10–21.
263 E. A. Clark and I. Fritsch, *Anal. Chem.*, 2004, **76**, 2415–2418.
264 P. U. Arumugam, E. S. Fakunle, E. C. Anderson, S. R. Evans, K. G. King, Z. P. Aguilar, C. S. Carter and I. Fritsch, *J. Electrochem. Soc.*, 2006, **153**, E185.
265 Z. P. Aguilar, P. Arumugam and I. Fritsch, *J. Electroanal. Chem.*, 2006, **591**, 201–209.
266 M. C. Weston, M. D. Gerner and I. Fritsch, *Anal. Chem.*, 2010, **82**, 3411–3418.
267 C. K. Nash and I. Fritsch, *Anal. Chem.*, 2016, **88**, 1601–1609.
268 F. Z. Khan and I. Fritsch, *J. Electrochem. Soc.*, 2019, **166**, H615–H627.
269 F. Z. Khan, J. A. Hutcheson, C. J. Hunter, A. J. Powless, D. Benson, I. Fritsch and T. J. Muldoon, *Anal. Chem.*, 2018, **90**, 7862–7870.
270 J. C. Sikes, K. Wonner, A. Nicholson, P. Cignoni, I. Fritsch and K. Tschulik, *ACS Phys. Chem. Au*, 2022, **2**, 289–298.
271 T. Cesin-AbouAtme, C. G. Lopez-Almeida, G. Molina-Labastida and J. G. Ibanez, *J. Chem. Educ.*, 2021, **98**, 3045–3049.
272 W. Zhang, K. Banerjee-Ghosh, F. Tassinari and R. Naaman, *ACS Energy Lett.*, 2018, **3**, 2308–2313.
273 C. Hunt, Z. Zhang, K. Ocean, R. P. Jansonius, M. Abbas, D. J. Dvorak, A. Kurimoto, E. W. Lees, S. Ghosh, A. Turkiewicz, F. A. Garcés Pineda, D. K. Fork and C. P. Berlinguette, *J. Am. Chem. Soc.*, 2022, **144**, 733–739.
274 Z. Bian, K. Kato, T. Ogoshi, Z. Cui, B. Sa, Y. Tsutsui, S. Seki and M. Suda, *Adv. Sci.*, 2022, **9**, 2201063.
275 I. Mogi and K. Watanabe, *Jpn. J. Appl. Phys.*, 2005, **44**, L199–L201.
276 I. Mogi, R. Aogaki and K. Watanabe, *Bull. Chem. Soc. Jpn.*, 2015, **88**, 1479–1485.
277 I. Mogi, R. Aogaki and K. Takahashi, *Magnetochemistry*, 2021, **7**, 142.
278 R. A. Rosenberg, D. Mishra and R. Naaman, *Angew. Chem., Int. Ed.*, 2015, **54**, 7295–7298.
279 R. Naaman and D. H. Waldeck, *Annu. Rev. Phys. Chem.*, 2015, **66**, 263–281.
280 K. Banerjee-Ghosh, O. Ben Dor, F. Tassinari, E. Capua, S. Yochelis, A. Capua, S.-H. Yang, S. S. P. Parkin, S. Sarkar, L. Kronik, L. T. Baczewski, R. Naaman and Y. Paltiel, *Science*, 2018, **360**, 1331–1334.
281 T. S. Metzger, S. Mishra, B. P. Bloom, N. Goren, A. Neubauer, G. Shmul, J. Wei, S. Yochelis, F. Tassinari, C. Fontanesi, D. H. Waldeck, Y. Paltiel and R. Naaman, *Angew. Chem., Int. Ed.*, 2020, **59**, 1653–1658.
282 K. Santra, D. Bhowmick, Q. Zhu, T. Bendikov and R. Naaman, *J. Phys. Chem. C*, 2021, **125**, 17530–17536.
283 H. Lee, H. Han and S. Jeon, *Anal. Chem.*, 2021, **93**, 12237–12242.
284 Y. Ikezoe and M. Sugaya, US20220181054, 2022.
285 K. Isai, M. Suwa and H. Watarai, *Anal. Sci.*, 2009, **25**, 1–3.
286 K. Miyamoto, K. Isai, M. Suwa and H. Watarai, *J. Am. Chem. Soc.*, 2009, **131**, 6328–6329.
287 M. Suwa, Y. Nakano, S. Tsukahara and H. Watarai, *Anal. Chem.*, 2013, **85**, 5176–5183.
288 M. Arase, M. Suwa and H. Watarai, *Anal. Chem.*, 2006, **78**, 6660–6663.
289 M. Arase, M. Suwa and H. Watarai, *Anal. Bioanal. Chem.*, 2008, **391**, 701–707.
290 Y. H. Matsuda, *Crystals*, 2020, **10**, 866.
291 S. Nimpf and D. A. Keays, *iScience*, 2022, **25**, 104454.
292 P. J. Hore and H. Mouritsen, *Annu. Rev. Biophys.*, 2016, **45**, 299–344.
293 G. Bao, *J. Appl. Mech.*, 2021, **88**, 1–7.
294 H. Watarai and Z. Chen, *Bull. Chem. Soc. Jpn.*, 2019, **92**, 949–951.
295 H. Watarai, S. Subhan Memon Sakurai and H. Subhan Memon Sakurai, *Anal. Sci.*, 2019, **35**, 951–954.
296 J. Luo and P. J. Hore, *New J. Phys.*, 2021, **23**, 043032.
297 V. Radu, J. C. Price, S. J. Levett, K. K. Narayanasamy, T. D. Bateman-Price, P. B. Wilson and M. L. Mather, *ACS Sens.*, 2020, **5**, 703–710.
298 S. Knappe, T. H. Sander, O. Kosch, F. Wiekhorst, J. Kitching and L. Trahms, *Appl. Phys. Lett.*, 2010, **97**, 133703.
299 O. Baffa, R. H. Matsuda, S. Arsalani, A. Prospero, J. R. A. Miranda and R. T. Wakai, *J. Magn. Magn. Mater.*, 2019, **475**, 533–538.